Vrije Universiteit Brussel

Faculteit Wetenschappen
en Bio-ingenieurswetenschappen
Vakgroep Fysica

# A search for supersymmetry in the four top quark final state at the CMS experiment

Proefschrift ingediend met het oog op het behalen
van de graad van Master in de Wetenschappen

Kevin Deroover

Promotor: Prof. Dr. Jorgen D'Hondt
Co-promotor: Dr. James Keaveney


Juni 2013

# Contents

# Introduction

Since the mid-1970s elementary particles together with their fundamental interactions are theoretically well described by the Standard Model of particle physics. In the past decades many aspects of this theory, such as the existence of quarks, neutrino's, the Z and W bosons and their fundamental interactions, have been experimentally validated. Anno 2013 the experimental validation of the Standard Model is completed with the discovery of the Brout-Englert-Higgs boson, making the Standard Model a very succesful theory. Even though the story of the Standard Model has reached its final chapter, it has fundamental shortcomings, such as the hierarchy problem, its inability to correctly incorporate gravity or describe dark matter. In order to be consistent with every aspect of the universe, the Standard Model has to be modified or an extension covering its failures has to be introduced. Out of the many theories proposed as an extension, Supersymmetry (SUSY) looks the most promising as it provides solutions to the hierarchy problem and dark matter by introducing a whole series of new particles. If such Supersymmetric particles exist, detectable signatures may be produced in energetic collisions.

Currently the Large Hadron Collider (LHC) at the CERN laboratory near Geneva is the most powerful accelerator in the world, colliding protons at a centre of mass energy of 8 TeV. Along the LHC four big particle detectors are placed to collect collision data for physics analysis. The Compact Muon Solenoid (CMS) is one of these detectors, built for a varied physics programme involving the search for Supersymmetric phenomena.

Top quarks are produced abundantly due to the large energy of the proton collisions and the high luminosity of the LHC. The top quark sector is very sensitive to new physics, as in the production and decay of these heavy quarks a large amount of energy is involved, which could lead to the production of energetic new physics phenomena such as Supersymmetry.

This thesis presents a procedure to search for Supersymmetric signals in the kinematics of final state topologies with four top quarks. By means of selection criteria, based on the topological properties of the process, the signal will be selected out of the large amount of Standard Model processes as much as possible to obtain a higher sensitivity for the signal. However, because the signal is a very rare process, such selection criteria do not give rise to the desired sensitivity, so a number of kinematic variables will be combined into a 'master' variable to increase the discrimination power between signal and Standard Model processes. Having obtained a discriminating master variable, the cross section of the signal process will be limited using statistical analysis tools in which simulations of the signal and

Standard Model processes are compared to the actual measured data at the CMS experiment.

Chapter 1 contains a description of the Standard Model, its failures and an introduction to Supersymmetry. Chapter 2 sketches the experimental setup of the Large Hadron Collider and the CMS experiment, which has the purpose of collecting collision data in order to probe the Standard Model and theories beyond. Further on, in Chapter 3, it is explained how the CMS experiment reconstructs fragments of the proton collisions in order to understand the collision at the most fundamental level. The several aspects of the simulations of proton collisions is also explained in Chapter 3. In Chapter 4 the Supersymmetric process this thesis looks for, is introduced. The procedure to discriminate this Supersymmetric signal from Standard Model processes is also discussed in Chapter 4. In Chapter 5 an upper limit on the cross section of the considered signal is calculated. Finally the conlusions of this analysis and an outlook to the future are given in Chapter 6.

# Chapter 1

# Elementary particle physics

## 1.1 The Standard Model

The fundamental constituents of nature and their interactions are described in the theory of the Standard Model (SM). The SM succeeds in combining three out of four fundamental forces into one consistent quantum gauge theory. A quantum gauge theory is a theoretical framework in which the quantum mechanical concepts of elementary particles and interactions are descibed by treating particles as excited states of their underlying physical fields. In such framework the interactions between elementary particles are propagated by force fields, also referred to as force carrieres. The three forces described in the SM are the weak, electromagnetic (also referred to as electroweak interactions) and strong force. This chapter will give a short introduction to the Standard Model, based on [1, 2].

### 1.1.1 Particle content and interactions

All visible matter in the universe is described by matter particles, called fermions, force carriers, called bosons. The fundamental difference between these types of particles is their spin; fermions carry half-integer spin, whereas bosons have integer spin. Every fermion has an anti-fermion having the same quantum properties, except for an opposite charge. Furthermore fermions can be classified into particles carrying colour charge[1], which are called quarks, and those who do not, which are called leptons. Fermions are categorized into three generations, each identical to the other except for mass.

The bosons representing the strong interactions are called gluons $g$, which are massless and carry colour charge. Another massless boson is the photon $\gamma$ which mediates the electromagnetic force. The third force described by the SM, the weak force, gives rise to three massive bosons: $W^{\pm}$- and $Z$ bosons. The fermions and gauge bosons of the SM are given in Figure 1.1.

Up to July 2012 the experimentally confirmed SM elementary particle content consisted only of fermions and gauge bosons. On July 4 2012 however a new particle

[1] The colour charge indicates the ability of a particle to interact via the strong force.

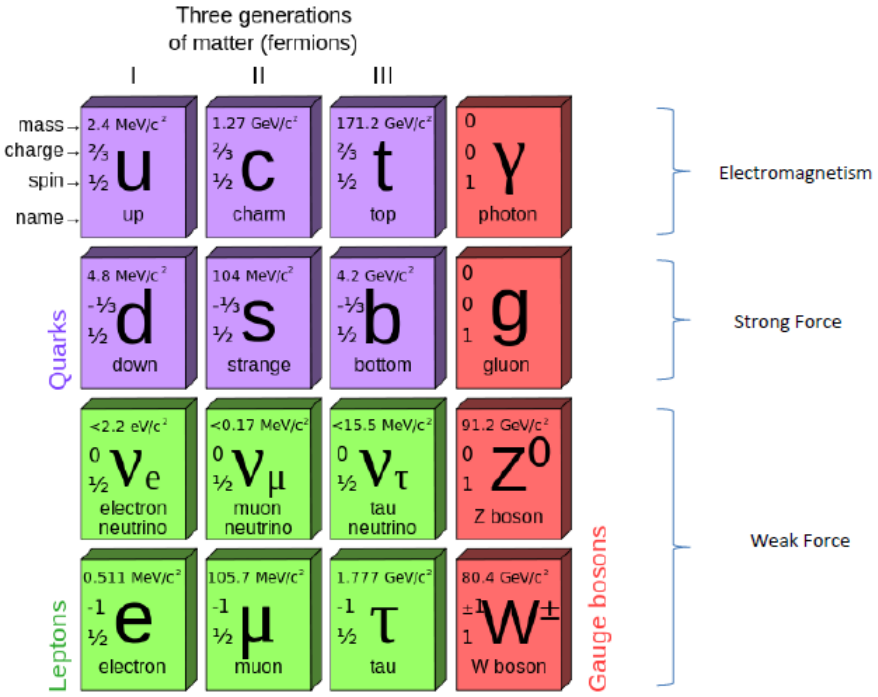


Figure 1.1: The fermions and gauge bosons of the Standard Model as taken from [3], with their experimentally confirmed properties as indicated.

was added, called the Brout-Englert-Higgs (BEH) boson, which was discovered at the Large Hadron Collider experiments with a mass of 125.3 ± 0.6 GeV/$c^2$ [4]. This particle was tentatively confirmed on March 4 2013 to be the BEH boson as theorized by R. Brout, F. Englert [5] and P. Higgs [6] (and others). The BEH boson, a scalar boson with no electric or colour charge, introduces rest-mass[2] to all bosons and elementary fermions without breaking gauge invariance.

### 1.1.2 Theoretical Framework

The theoretical framework of the SM is a quantum gauge theory, as explained above. The dynamics and kinematics of the particle and force fields in the theory are controlled by a Lagrangian $\mathcal{L}$. The Lagrangian of the SM is constructed such that it contains a certain set of symmetries which represent physics conservation laws as described by Noether's theorem [7]. Conservation of energy, momentum, angular momentum and charge are just a few examples of conservation laws coming from symmetries, which need to be represented in the SM Lagrangian. In order to sustain such symmetries under local group transformations, *gauge invariance* is imposed.

[2] Note that the real mass as observed in the macroscopic world is mainly caused by the binding energy coming from the strong force. The BEH boson is only responsible for the rest-mass to the elementary particles.

### Gauge invariance

Consider for example the wave function of a spin-1/2 fermion with mass m to be a Dirac spinor $\psi(x)$, for which the Lagrangian in natural units ($\hbar$ = c = 1) is

$$\mathcal{L}_{\text{Dirac}} = i\bar{\psi}\gamma^{\mu}\partial_{\mu}\psi - m\bar{\psi}\psi, \tag{1.1}$$

with $\gamma^{\mu}$ the Dirac matrices[3] and $\bar{\psi} = \psi^{\dagger}\gamma^{0}$ with $\psi^{\dagger}$ the hermitian conjugate of $\psi$. This Lagrangian is invariant under global phase transformations ($\psi$(x) $\rightarrow$ $\psi$'(x) = $e^{ig\alpha}$ $\psi$(x), with $\alpha$ constant). Now consider a *local* phase transformation represented by the unitary matrix U($\alpha$) of a group acting on the fermion field as

$$\psi(x) \rightarrow \psi'(x) = U(\alpha(x))\psi(x) = e^{ig\alpha(x)^{\nu}T_{\nu}}\psi(x), \tag{1.2}$$

with $\alpha^{\nu}$ the transformation parameters, $T_{\nu}$ the generators of the group and g a real constant. Implicit summation over $\nu$ is suggested in this notation, where $\nu$ runs from 1 to the dimension of the group (i.e. the number of generators). Inserting (1.2) in (1.1) one gets the following Lagrangian:

$$\mathcal{L}_{\text{Dirac}} - g\bar{\psi}(x)\gamma^{\mu}\psi(x)\partial_{\mu}(\alpha^{\nu}(x)T_{\nu}). \tag{1.3}$$

Consequently the Dirac Lagrangian as defined in (1.1) is not invariant under local transformations. To restore the internal symmetry, the partial derivative is replaced with a covariant derivative, defined by

$$\mathcal{D}_{\mu} = \partial_{\mu} - igT_{\nu}A^{\nu}_{\mu}, \tag{1.4}$$

with $A^{\nu}_{\mu}$ introduced as gauge boson fields. For the covariant derivative to be invariant under the group transformation, it has to transform like the fields, i.e. $\mathcal{D}'_{\mu}\psi' =$ U $\mathcal{D}_{\mu}\psi$. This requirement determines the transformation laws of the gauge fields as

$$T_{\nu}A^{\nu'}_{\mu} = e^{ig\alpha(x)^{\nu}T_{\nu}}T_{\nu}A^{\nu}_{\mu}e^{-ig\alpha(x)^{\nu}T_{\nu}} - \frac{i}{g}e^{ig\alpha(x)^{\nu}T_{\nu}}\partial_{\mu}(e^{-ig\alpha(x)^{\nu}T_{\nu}}). \tag{1.5}$$

The second term in this gauge transformation will cancel the last term in (1.3), making the Lagrangian invariant under local phase transformations. This whole process is referred to as imposing gauge invariance on a Lagrangian.

Substituting (1.4) into (1.1) gives

$$\mathcal{L}_{\text{Dirac}} = i\bar{\psi}\gamma^{\mu}\partial_{\mu}\psi - m\bar{\psi}\psi + g\bar{\psi}\gamma^{\mu}T_{\nu}A^{\nu}_{\mu}\psi. \tag{1.6}$$

This Dirac Lagrangian lead to the development of quantum electrodynamics (QED) in which the transformation of the Lagrangian is considered under the Abelian group[4] U(1) and is the starting point of the SM. The corresponding interpretation of the gauge field $A_{\mu}(x)$ has lead to the prediction of the photon. The Dirac

[3] The Dirac matrices are 4 × 4 matrices, defined by $\{\gamma^{\mu}, \gamma^{\nu}\} = 2\eta^{\mu\nu}$ with $\eta^{\mu\nu}$ = diag(+—) the Minkowski metric. The notation {a,b} denotes the anti-commutator, i.e. $ab + ba$.

[4] In an Abelian group the generators $T_{\nu}$ commute, whereas in non-Abelian groups the commutator of generators is not zero, e.g. in SU(2) $[T_{\nu}, T_{\mu}] = i\sum_{i}^{3}\epsilon^{\mu\nu\gamma}T_{\gamma}$ with $\epsilon^{\mu\nu\gamma}$ the Levi-Civita symbol.

Lagrangian describes the propagation of free electrons (first two terms) and their interactions through photons (third term). The interaction strength between fermions and gauge bosons is defined by 'g', called the *coupling constant*. These interactions are schematically represented as *Feynmann diagrams*, in which the point where several particles meet is called a *vertex*. Based on the Feynman diagrams a number of rules are constructed, called Feynman rules, to calculate matrix elements for cross sections of interaction and decay processes.

In order to be in agreement with experimental results and to get a renormalisable theory, meaning that the physical predictions in terms of a finite number of free parameters remain finite, the SM combines three symmetry groups into one gauge symmetry group

$$SU(3)_c \otimes SU(2)_L \otimes U(1)_Y. \tag{1.7}$$

The connection between the fundamental forces and these three symmetry groups will be further discussed.

### Electroweak theory

The electroweak theory (EW) is described by requiring gauge invariance in the $SU(2)_L \otimes U(1)_Y$ group. The non-Abelian group $SU(2)_L$ has three generators, introducing three gauge fields $\mathrm{W}_\mu^\alpha$ ($\alpha \in \{1,2,3\}$). The subindex L indicates that the gauge fields only couple to left-handed[5] fermions, as required by the observed parity violating nature of the weak force. The left-handed fermions are grouped in *doublets* (e.g. the doublet $(e_L,\nu_{eL})$) in the SM, while the right-handed fermions remain isolated in *singlets*. The Abelian group $U(1)_Y$ has one generator, namely the hypercharge Y, leading to only one gauge field $\mathrm{B}_\mu$. Two coupling constants are introduced in this gauge symmetry group, namely $g_1$ for $U(1)_Y$ and $g_2$ for $SU(2)_L$.

The physically observable gauge bosons of the electroweak theory, like the photon field $\mathrm{A}_\mu$ and the $\mathrm{Z}_\mu^0$- and $\mathrm{W}_\mu^\pm$-fields, are superpositions of the four gauge fields of $SU(2)_L \otimes U(1)_Y$:

$$A_\mu = \sin\theta_\mathrm{W} \mathrm{W}_\mu^3 + \cos\theta_\mathrm{W} \mathrm{B}_\mu, \tag{1.8}$$

$$Z_\mu = \cos\theta_\mathrm{W} \mathrm{W}_\mu^3 - \sin\theta_\mathrm{W} \mathrm{B}_\mu, \tag{1.9}$$

$$W_\mu^\pm = \sqrt{\frac{1}{2}}(W_\mu^1 \mp i W_\mu^2), \tag{1.10}$$

with $\theta_W$ the weak mixing angle, defined as

$$\tan\theta_\mathrm{W} = \frac{\mathrm{g_1}}{\mathrm{g_2}}. \tag{1.11}$$

The strength of flavour changing weak decays of quarks are represented in the CabibboKobayashiMaskawa matrix (CKM matrix) [8]. The elements $|V_{qq\prime}|^2$ of the CKM matrix represent the probability of a quark with flavour q to decay through weak interactions to a quark with flavour q$\prime$.

[5] The handedness or *chirality* of a Dirac fermion field is defined as $\psi_L = \frac{1}{2}(1-\gamma_5)\psi$ for left-handed fermions and $\psi_R = \frac{1}{2}(1+\gamma_5)\psi$ for right-handed fermions, with $\gamma^5 = i\gamma^0\gamma^1\gamma^2\gamma^3\gamma^4$

### Quantum Chromodynamics (QCD)

Quantum chromodynamics is represented in the Standard Model by the non-Abelian group $SU(3)_c$. This group group has eight generators and thereby eight associated gauge boson fields $G_\mu^\alpha$ ($\alpha \in \{1,2,..,8\}$), which are massless and known as the physical gluon fields. The subindex c denotes the fact that QCD only describes the interactions of colour carrying particles, namely gluons[6] and quarks. The conventional names for the colour charges are *red*, *green* and *blue* and their anti-colours. The coupling constant representing QCD will be denoted as $g_3$.

An important characteristic of QCD is asymptotic freedom, which states that the strong coupling constant becomes weaker as the energy increases and stronger as the distance increases. This phenomena results in *colour confinement*, meaning quarks and gluons can not exist on their own and will never be observed as individual particles. Instead all quarks and gluons are bound in colour-neutral states called *hadrons*. Hadrons are subcategorized into *mesons*, made of two quarks (e.g. $\pi^0$, $K^0$), and *baryons*, made of three quarks (e.g. proton, neutron). The main impact of colour confinement is the fragmentation or hadronization of individual quarks and gluons. Fragmentation of individual quarks and gluons is described by several models. One of these models is the string fragmentation model [9]. This model is based on the physical image of a narrow colour tube connecting two quarks/gluons of which the stored energy increases with distance. If the tube is then stretched out too far it breaks and a new quark/gluon pair is formed.

### Electroweak symmetry breaking

So far the SM does not contain mass terms for the elementary particles, which is in direct conflict with observations. Such mass terms can not be introduced explicitely, because this would break gauge invariance, so in order to accomodate mass for the massive bosons of the SM in a gauge invariant way, a complex scalar doublet $\phi$ is introduced, with a non-zero vacuum expectation value (VEV) $v$. The introduction of the scalar doublet induces an interaction between $\phi$ and the massive boson fields, giving rise to mass terms in the Lagrangian, which are gauge invariant. In a similar way, mass is given to fermions by adding interaction terms between $\phi$ and the fermionic fields in the Lagrangian. The coupling strength between $\phi$ and the fermion fields is quantified by the Yukawa couplings. The complex scalar doublet gives rise to one physically observable particle, called the Brout-Englert-Higgs boson.

With the introduction of all gauge fields and coupling constants, the total co-

[6] The fact that gluons carries colour is a direct consequence from the fact that SU(3) is non-Abelian, inducing self-interactions on the gluons.

variant derivative (1.4) for the SM becomes

$$D_\mu = \partial_\mu + ig_1\frac{Y}{2}B_\mu + ig_2\frac{\tau^a}{2}W_\mu^a + ig_3\frac{\lambda^a}{2}G_\mu^a, \tag{1.12}$$

with $Y$, $\tau^a$ and $\lambda^a$ respectively the hypercharge, Pauli matrices and the Gell-Mann matrices representing the generators of respectively $U(1)_Y$, $SU(2)_L$ and $SU(3)_c$. The full Lagrangian describing the SM arises by writing down the Dirac terms for the fermions (1.1) and replacing the partial derivative by the covariant derivative defined by the gauge symmetry group $SU(3)_c \otimes SU(2)_L \otimes U(1)_Y$ (1.12). Also the electroweak symmetry breaking sector is accounted fo by adding kinetic and potential terms for the scalar doublet, together with the Yukawa coupling terms for fermion fields. Finally kinetic terms for the gauge fields are included to provide a description of the propagation of free gauge bosons.

### 1.1.3 Failures of the Standard Model

The SM is not a perfect theory and fails to provide a full description of nature. First of all the theory only succesfully combines three out of four fundamental forces. By not accounting for the gravitational force, the SM does not describe phenomena where quantum and gravitational effects are simultaneously important, such as at the Big Bang or the center of black holes.

Another flaw, known as the *hierarchy problem* [10], is the inability to explain the large gap between the electroweak symmetry breaking scale ($\sim 10^2$ GeV/c$^2$) and the Planck scale ($\mathrm{m}_{Planck} \approx 10^{18}$ GeV/c$^2$). The hierarchy problem becomes most apparent when calculating the BEH boson mass to all orders of perturbation:

$$m_H^2 = (m_H^2)_0 + \Delta m_H^2, \tag{1.13}$$

with $\mathrm{m}_H$ the real physical mass of the BEH boson, $(\mathrm{m}_H)_0$ its bare mass and $\Delta\mathrm{m}_H$ the quantum loop corrections. The quantum loop correction to the BEH boson mass due to fermions in the loop is given by

$$(\Delta m_H^2)_f = N_f\frac{|\lambda_f|^2}{8\pi^2}\left(-\Lambda_{UV}^2 + 6m_f^2 log\left(\frac{\Lambda_{UV}}{m_f}\right) - 2m_f^2\right) + \mathcal{O}(1/\Lambda_{UV}^2), \tag{1.14}$$

with $\mathrm{N}_f$ the fermionic degree of freedom, $\mathrm{m}_f$ the fermion mass, $\lambda_f$ its Yukawa coupling and $\Lambda_{UV}$ the ultraviolet cut-off[7]. The most dominant contribution comes from the top quark, which has the largest Yukawa coupling to the scalar field caused by its large mass. If the SM is the only physics theory up to the Planck scale, the cut-off would be $\Lambda_{UV} = \mathrm{m}_{Planck}$. In that case, in order for the theorised prediction to agree with the experimentally measured mass ($\mathrm{m}_H \approx 125$ GeV/c$^2$), a fine-tuning cancellation between the bare mass and the quantum loop corrections of over 30 orders of magnitude is needed, which is unnatural.

Another important consequence of the hierarchy problem is the scaling of the three coupling constants $g_1$, $g_2$ and $g_3$ to the energy scale with which infinities are

[7] $\Lambda_{UV}$ is a cut-off parameter introduced to regulate divergent integrals arising from quantum loops at higher order calculations.

regulated, referred to as the renormalisation scale. This phenomena is also known as the running of coupling constants. Grand Unified Theories (GUTs) [11] aim to unify all forces at a certain energy scale, such that there is only one coupling constant at that energy scale, the GUT scale. In order to accomplish the idea of unification, these three SM coupling constants should be equal at a certain value for the renormalisation scale. The SM however does not predict such a unification, but instead predicts that the coupling constants meet at different values for the renormalisation scale.

An issue which is also not addressed by the SM is the existence of non-baryonic cold dark matter and dark energy, making up respectively 23% and 72% of the universe's energy density. Cold dark matter is presumably only sensitive to the weak and gravitational force. Since the only known SM particles with these characteristics are neutrinos, being too light to accomodate this great amount of dark matter, other models are needed to accomodate such Weakly Interacting Massive Particles (WIMPs).

Some other issues the SM also struggles with are for example: why are there exactly three generations? Is it possible to predict the values of all 19 free parameters[8] in the theory? Why is CP violation[9] so strong...?

All these failures indicate that the SM is expected to break down at higher energies. This encourages the idea to look at physics beyond the Standard Model.

## 1.2 Beyond the Standard Model

Many different theories have been constructed in order to solve the SM problems, such as Extra Dimensions, Technicolour, Supersymmetry... Out of all these theories, supersymmetry is one of the most promising as it provides a candidate for dark matter, solves the fine tuning problem in the BEH mass and adjusts the running of coupling constants to the extent that they become unified at the GUT scale. In this section SUSY will be introduced on a very basic level, based on the ideas presented in [12, 13].

### 1.2.1 Supersymmetry

SUSY is established by requiring an additional spacetime symmetry, which connects bosonic fields to fermionic fields as

$$Q|boson>=|fermion>, \qquad Q|fermion>=|boson>, \tag{1.15}$$

[8] These parameters are: 3 coupling constants ($g_1$, $g_2$ and $g_3$), 2 parameters from the Higgs sector, 9 masses of the quarks and leptons, 4 parameters related to flavour mixing in the CKM matrix and 1 related to QCD. The number of free parameters can even be increased when taking the neutrino mass giving mechanism into account.

[9] Charge conjugation Partiy symmetry or CP symmetry dictates that the laws of physics are invariant if a particle is interchanged with its anti-particle. The violation of CP symmetry is strongly correlated to the fact that matter is more abundantly present in the universe than anti-matter.

with $Q$ the supersymmetric generator. Bosons and fermions which transform into each other according to the supersymmetric generator are grouped in irreducible representations called *superfields*. All particles in the same superfield are called *superpartners* of each other. The supersymmetric generator Q is constructed such that the superpartners of fermions are scalar bosons and the superpartners of gauge/scalar bosons are fermions, meaning Q carries spin 1/2.

It can be proven that the generators Q and $Q^\dagger$ commute with the four momentum generator of spacetime $P_\mu$ ($[P_\mu,Q_\nu] = 0 = [P_\mu,Q_\nu^\dagger]$) and also with the generators of gauge symmetry groups. These commutation relations are part of the basic SUSY algebra. The commutation of Q with P straightforwardly leads to the fact that superpartners have equal masses. Knowing that the eigenvalue of $P^2$ corresponds to the mass, this is easily proven by

$$P^2|particle >= P^2Q|superparticle >= QP^2|superparticle >, \tag{1.16}$$

In a similar way, the fact that Q commutes with the generators of the gauge symmetry groups is used to show that superpartners will behave similarly under gauge transformations, therefore having the same colour-, electric- and weak hypercharge. It can also be shown that in a superfield the number of bosonic degrees of freedom equals the number of fermionic degrees of freedom.

### Supersymmetric extension of the Standard Model

None of the existing SM particles can be linked as a superpartner to another SM particle and therefore new particle fields have to be introduced in SUSY extensions to the SM. The symbol convention for superpartners of SM particles is the SM symbol with a tilde on top, e.g. the superpartner of a gluon is indicated as $\tilde{g}$. The superpartners of SM fermions are named scalar fermions (or *sfermions*), e.g. the superpartner of a left-handed electron ($e_L$) is called a $left-handed\ selectron$ [10] ($\tilde{e_L}$). Superpartners of SM gauge bosons get the suffix 'ino' after the SM name, e.g. the superpartner of the Z boson is a *Zino* ($\tilde{Z}$).

The most straightforward extension of the Standard Model by means of SUSY is the *Minimal Supersymmetric Standard Model* (MSSM). The particle content of its first generation is listed in Table 1.1. An important feature of the MSSM is the introduction of one extra scalar doublet to the SM next to original scalar doublet, which is necessary to maintain gauge invariance in the SUSY Lagrangian.

Table 1.1 lists the particle fields as they appear in the Lagrangian of the MSSM. The real physically observable particles are superpositions of these fields. The superposition of the Bino, neutral Wino ($\tilde{W}^0$) and neutral Higgsinos ($\tilde{H}_u^0$ and $\tilde{H}_u^0$) lead to the physical mass eigenstates called *neutralinos* of which there are four: $\tilde{\chi}_1^0$, $\tilde{\chi}_2^0$, $\tilde{\chi}_3^0$, $\tilde{\chi}_4^0$. In the same way the charged Wino's and Higgsinos are combined into four physical *charginos*: $\tilde{\chi}_1^\pm$, $\tilde{\chi}_2^\pm$.

[10] Note that the left-handed selectron actually does not carry any chirality, since it is a scalar. The handedness of this scalar just indicates the chirality of its superpartner.

Table 1.1: The particle field content of the MSSM.

| SM particle | | spin | superpartner | | spin |
|---|---|---|---|---|---|
| quarks | $(u_L\ ,\ d_L)$ | $\frac{1}{2}$ | squarks | $(\tilde{u}_L\ ,\ \tilde{d}_L)$ | 0 |
| | $u_R$ | $\frac{1}{2}$ | | $\tilde{u}_R$ | 0 |
| | $d_R$ | $\frac{1}{2}$ | | $\tilde{d}_R$ | 0 |
| leptons | $(\nu\ ,\ e_L)$ | $\frac{1}{2}$ | sleptons | $(\tilde{\nu}\ ,\ \tilde{e}_L)$ | 0 |
| | $e_R$ | $\frac{1}{2}$ | | $\tilde{e}_R$ | 0 |
| W bosons | $W^{\pm}\ W^0$ | 1 | Wino's | $\tilde{W}^{\pm}\ \tilde{W}^0$ | $\frac{1}{2}$ |
| B | $B$ | 1 | Bino | $\tilde{B}$ | $\frac{1}{2}$ |
| gluons | $g$ | 1 | gluinos | $\tilde{g}$ | $\frac{1}{2}$ |
| BEH | $(H_u^+,\ H_u^0)$ | 0 | Higgsinos | $(\tilde{H}_u^+,\ \tilde{H}_u^0)$ | $\frac{1}{2}$ |
| | $(H_u^+,\ H_u^0)$ | 0 | | $(\tilde{H}_u^+,\ \tilde{H}_u^0)$ | $\frac{1}{2}$ |

### Supersymmetry breaking

As stated above SUSY predicts the existence of new particles which have some of the same properties as their SM counterparts, including equal mass. The major issue with this prediction is that, if it were true, such particles would have been detected by now, since their masses are well within the energy range of previous accelerators. Therefore SUSY needs to be broken such that the masses of superparticles are increased to a scale where they remain undetectable for low energy accelerators. Several breaking mechanisms exist, leading to different models for SUSY, such as minimal supergravity (mSUGRA) [14] and gauge-mediated SUSY breaking (GMSB) [15]

Though the theories on how to break SUSY, in general the breaking mechanism in the MSSM is proposed to be a $soft$ SUSY breaking, meaning it does not introduce quadratic divergences and ensures a renormalisable Lagrangian. The explicit soft breaking for the MSSM is in general introduced as an extra term in the Lagrangian as

$$\mathcal{L}_{MSSM} = \mathcal{L}_{chiral} + \mathcal{L}_{gauge} + \mathcal{L}_{gauge-interactions} + \mathcal{L}_{breaking}. \tag{1.17}$$

The first and second term describe the behaviour of chiral and gauge fields (including those of the SM), the third term concerns the allowed gauge interactions. Such soft SUSY breaking introduces 105 new parameters, which make it difficult to experimentally discover or exclude even very simple SUSY models. Several assumptions can be made which reduce the number of parameters, such as assuming the first and second generation sfermions are the same at low energy. SUSY models that depend on less parameters are easier to study from an experimental point of view.

**Predictions of the MSSM**

The predictions of the MSSM provide solutions to several of the unsolved riddles in the SM. The most important solution is provided by the extra quantum corrections to the BEH boson mass (1.13) introduced by the sfermions, which is a scalar contribution given by [10]

$$(\Delta m_H^2)_s = \frac{\lambda_s N_s}{16\pi^2}\left(-\Lambda_{UV}^2 + 2m_s^2 log\left(\frac{\Lambda_{UV}}{m_s}\right)\right) - \frac{\lambda_s^2 N_s v}{16\pi^2}\left(-1 + 2log\left(\frac{\Lambda_{UV}}{m_s}\right)\right) + \mathcal{O}(1/\Lambda_{UV}), \tag{1.18}$$

with $N_s$ the number of scalar particles, $m_s$ the mass of the scalar and $\lambda_s$ the coupling of the scalar to the scalar BEH field. This contribution cancels the quadratic divergence $\Lambda_{UV}^2$ in (1.14) if for every fermion there are two scalars with $\lambda_f^2 = \text{-}\lambda_s$. This is the case in the MSSM, where for every fermion a complex scalar exists (containing two real scalar bosons $N_s = 2\ N_f$), having the same quantum numbers including the coupling[11] $\lambda$. Although the quadratic divergences disappear, the less problematic logarithmic divergence remains as

$$\frac{\lambda_f^2 N_f}{4\pi^2}\left((m_f^2 - m_s^2) log\left(\frac{\Lambda_{UV}}{m_s}\right) + 3m_f^2 log\left(\frac{m_s}{m_f}\right)\right). \tag{1.19}$$

Thus the residual logarithmic divergence maintains the need for fine tuning. However, the level of necessary fine tuning can now be adjusted by requiring certain limits on the masses of the scalar superpartners of fermions. It is calculated that in order for the bare BEH mass $m_0$ to be of the order of the experimental mass, the stop quark has to be lighter than 1 TeV/$c^2$. The effect of fine-tuning requires less drastic bounds on the masses of first and second generation squarks, which can be a factor of 5 or more heavier than the stop quark, because they have much weaker Yukawa couplings than the top supermultiplet.

The MSSM also provides a candidate for the cold dark matter WIMP, by introducing a new symmetry called $R-parity$ defined as

$$R = (-1)^{3B+L+2s}, \tag{1.20}$$

with 'B' the baryon number, 'L' the lepton number and 's' the spin of the particle. This symmetry is introduced to ensure that baryon and lepton[12] violating terms in SUSY are very weak. R-parity is introduced such that SM particles have R = +1 and their superpartners R = -1. This new symmetry implies that in collisions of SM particles, superparticles are always produced in pairs. Another direct consequence of R-parity conservation is the prediction of a stable superparticle, which can not decay into SM particles. Such a stable superparticle can be found at the end of every superparticle decay chain, therefore by defintion being also the *Lightest*

[11] The statement $|\lambda_f^2| = \lambda_s$ is accomplished by the fact that scalar bosons contribute via one coupling to the BEH boson mass, whereas fermionic loops interact through two couplings with the scalar field.

[12] Baryon and lepton numbers are experimentally confirmed conserved quantities in the SM.

*Supersymmetric Particle* (LSP). Depending on the SUSY breaking mechanism, the LSP could be the lightest neutralino $\chi_1^0$, meaning it only interacts weakly and gravitationally with other particles, making it a candidate for cold dark matter.

Another interesting feature of the MSSM is its contribution to the unification of the three coupling constants $g_1$, $g_2$ and $g_3$. By increasing the number of particles the slope of the evolution of coupling constants is altered. If the masses of the superparticles are of the order of 1 TeV, the three couplings meet at one point, completing the unification of all forces at the grand unification scale $m_{GUT} = 10^{16} GeV/c^2$. This is visualised in Figure 1.2.

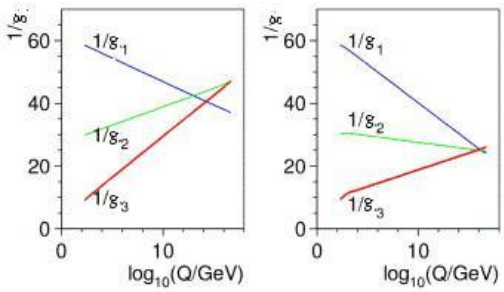


Figure 1.2: Visualisation of the running of coupling constants in the SM (left) and the change in slope by adding new particles in the MSSM (right).

### 1.2.2 Simplified Model Spectra

The first years in which the Large Hadron Collider experiments collected data (2010-2011), SUSY had mainly been tested in terms of model specific searches, such as the constrained MSSM (cMSSM) [16]. Although the cMSSM provides a simplified approach to SUSY, which reduces the numbers of parameters drastically and allows an easy comparison between theoretical prediction and experimental measurement, its predictions are not indicative for all MSSM or extensions.

Since there are many different SUSY breaking mechanisms and in order to do a relative model blind SUSY search, a simplified approach has been adopted, called *Simplified Model Spectra* (SMS) [17]. In such SMS a limited set of MSSM particles and decay chains is considered to produce certain topological signatures. The production amplitudes only depend on the masses of the involved particles and their branching ratios to other particles. Such a simplified strategy allows a SUSY search covering several MSSM theories, providing limits to several theories with just one search. The SMS adopts the same naming conventions as in the MSSM: gluino ($\tilde{g}$), squark ($\tilde{q}$), neutralino ($\tilde{\chi}^0$) and chargino ($\tilde{\chi}^{\pm}$). Also some of the consequences of R-parity conservation are imposed to some SMS (e.g. the existence of a LSP). The LSP is interpreted as a neutralino $\tilde{\chi}^0$ or gravitino $\tilde{G}$, which is the superpartner of the gravitation mediating particle called 'graviton'. The produced particles decay directly to the LSP and SM particles or to an on-shell intermediate particle, which then further decays to the LSP and SM particles.

Every SMS is labeled with 'TNx', where T refers to topology, N a number from 1 to 6 and x a string indicating the final state. The number is an indication for the

production mechanism; squark or gluino production decaying directly or indirectly to the final state x. The analysis presented in this thesis searches for the T1tttt, where two gluinos are produced in proton collisions and the gluinos have a direct three-body decay ($\tilde{g} \to t\bar{t}\tilde{\chi}_1^0$) and produce a final state containing four top quarks. This topology is schematically represented in Figure 1.3.

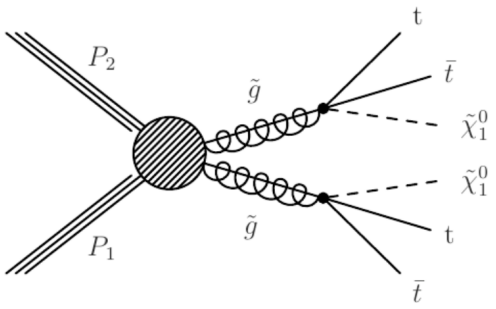


Figure 1.3: Diagram of the T1tttt channel.

# Chapter 2

# The Large Hadron Collider

The experimental environment in which this analysis is set, is the CMS experiment at the Large Hadron Collider (LHC [18]). The Large Hadron Collider is constructed with the sole purpose of doing fundamental physics research at the smallest scales, by recreating high energy collisions. This opens the experimental hunt for phenomena beyond the Standard Model, but also precise measurements of known phenomena. After having fulfilled its first goal, namely discovering the Higgs boson as the last missing link of the Standard Model, the Large Hadron Collider experiments will mainly concentrate on beyond the Standard Model searches, such as superymmetry.

## 2.1 The Large Hadron Collider

The basic principles of the LHC presented here are based on [19].

The LHC is a particle accelerator located at the European Organization for Nuclear Research (CERN) near Geneva at the French-Swiss border. The accelerator's complex is located in an underground circular tunnel with a circumference of 26.7 km. The LHC consists of two beampipes in which the protons are accelerated in opposite directions by superconducting radiofrequency (RF) cavities [20]. Those RF cavities also divide the protons into bunches. Along the beampipes 1232 superconducting dipole magnets ensure the circular path of both opposite proton beams. Another type of magnets, called quadrupoles, focus the bunches to the desired transverse size. The LHC is cooled down to 1.9K with liquid helium in order to reach the superconducting state for the magnets.

Designed to provide proton collisions at a centre of mass energy $\sqrt{s} = 14$ TeV, the LHC intends to achieve a luminosity $\mathcal{L}$ of $10^{34}\text{cm}^{-2}\text{s}^{-1}$. The luminosity in collider experiments is determined as

$$\mathcal{L} = f\frac{n_1 n_2}{4\pi\sigma_x\sigma_y}, \tag{2.1}$$

with f the bunch crossing frequency, $n_1$ and $n_2$ the number of particles in the colliding bunches and $\sigma_x$ and $\sigma_y$ the width of the bunches in the beam. In order to achieve

the proposed luminosity, the bunches contain $10^{11}$ particles and have a transverse size of about $17\mu m$. The bunch crossing frequency is about $(25\text{ ns})^{-1}$. The rate N at which particles collide is

$$N = \mathcal{L} \times \sigma, \tag{2.2}$$

with $\sigma$ the cross section of a particular process.

In order to achieve higher energy collisions than before hadrons are chosen instead of electrons. This choice is based on the arguments of energy loss due to synchrotron radiation[1], for which the effect is smaller for heavier particles. Although the proton can be accelerated to higher energies, it has less favourable properties compared to the electron due to its internal constituents called *partons*, which is a collective term for gluons and quarks. When protons collide, the fundamental collision is represented by the partons carrying only a fraction 'x' of the total momentum of the proton, so the actual fundamental centre of mass energy is defined as

$$\sqrt{s_{real}} = \sqrt{x_1 x_2 s}. \tag{2.3}$$

These momentum fractions are determined by the *parton density functions* (PDFs) f(x,$p_i$), which represent the probability parton 'p' with flavour 'i' emerges from the proton with a momentum fraction 'x'.

From 2010 to the end of 2011 the LHC has been continually colliding proton beams at a centre of mass energy of $\sqrt{s} = 7$ TeV and has delivered an integrated luminosity of over 5 $\text{fb}^{-1}$, making it the most powerful and highest energy particle accelerator in the world. After the first technical winter stop of 2012, the beam energy was increased to 4 TeV, giving centre of mass collisions of $\sqrt{s} = 8$ TeV and an integrated luminosity of over 23 $\text{fb}^{-1}$. Currently the LHC is at a shutdown until 2015 in order to upgrade the proton beam energy to reach the initially intended 7 TeV. This analysis uses the 2012 data recorded at $\sqrt{s} = 8$ TeV.

### The CERN accelerator complex

The protons go through a whole pre-acceleration process before being injected in the LHC. This pre-acceleration process is part of the CERN acceleratopr complex, which is shown in Figure 2.1. Firstly the protons are accelerated to an energy of 50 MeV with a linear accelerator (LINAC2), after which they enter the Proton Synchrotron Booster (PSB) reaching an energy of 1.4 GeV. Afterwards they are injected into the Proton Synchrotron (PS) increasing the energy to 26 GeV with which they reach the final stage of pre-acceleration, the Super Proton Synchrotron (SPS). In this final stage the protons are accelerated to 450 GeV and injected in opposite directions in the two separate beamlines of the LHC.

There are four interaction points along the LHC ring where the bunches cross over and provide collisions. Along those interaction points the four main experiments of the LHC are located: CMS [22], ATLAS [23], ALICE [24] and LHCb [25].

[1] The energy loss due to synchrotron radiation corresponds to $\Delta E \propto \frac{E^4}{Rm^4}$, with E the energy, R the radius of the accelerator and m the mass of the particle.

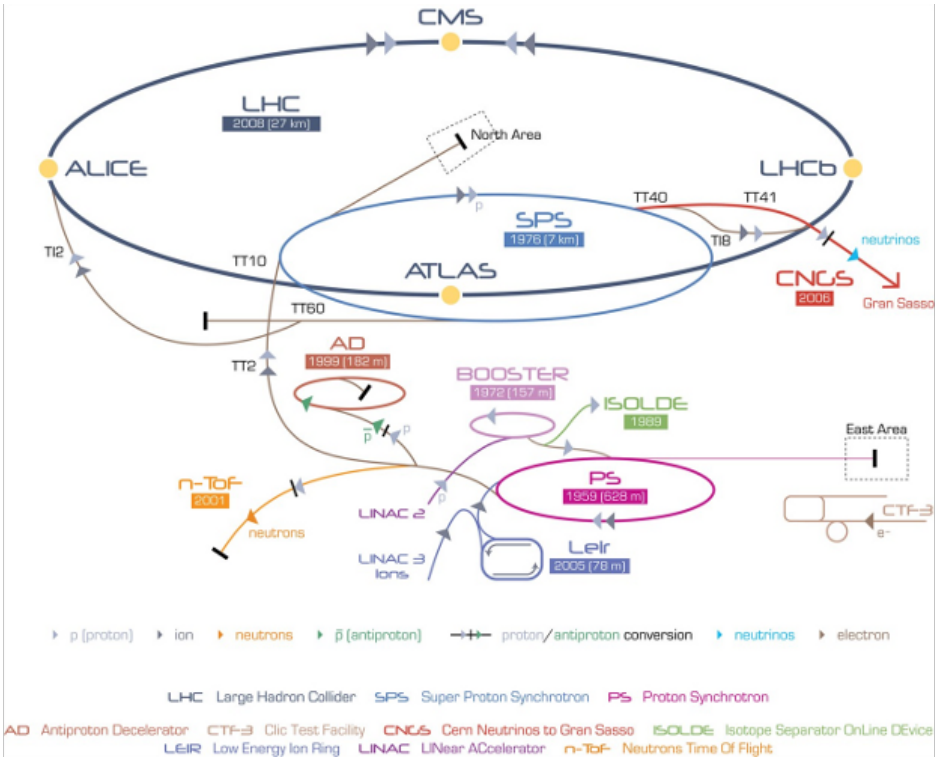


Figure 2.1: The CERN accelerator complex and main experiments, taken from [21].

The CMS and ATLAS experiments both are general physics experiments relying on different detector setups and techniques to study a large variety of physics phenomena, such as CP-violation, SM phenomena and beyond the SM physics. The ALICE eperiment looks into heavy ion collisions to study quark-gluon plasma's[2]. The LHCb experiment studies the difference between matter and anti-matter through b-quark physics. At the CMS interaction point a smaller experiment, called TOTEM [26], measures elastic scatterings, diffractive processes and total cross sections of proton collisions. Next to the ATLAS detector, the LHCf [27] experiment measures forwardly produced neutral particles in order to understand the interactions of cosmic rays in the atmosphere. Besides the LHC experiments mentioned here, many more experiments are conducted at the CERN instute, as indicated in Figure 2.1.

## 2.2 The Compact Muon Solenoid experiment

All illustrations in this chapter are taken from [3, 28].

The Compact Muon Solenoid (CMS) experiment, being a general purpose experiment, is optimised to measure every aspect of proton collisions. Its main characteristic is a cylindrical superconducting solenoid generating a magnetic field of 3.8 T, which is used to determine the momentum of a charged particle. The curvature of a charged particle trajectory in a magnetic field of known strength determines its momentum. In order to achieve the superconducting state of the magnet, the

[2] A state of matter existing shortly after the Big Bang.

solenoid is cooled down to 4.8 K using liquid helium. Together with the measured momentum, the muon chambers, electromagnetic- and hadronic calorimeters, are used to identify the produced particles and measure their four-momenta. Because the detector has to cope with a large instantaneous luminosity, the used materials are radiation hard and the detector has a high granularity. Compared to its total weight of 12500 tons and to other experiments, such as ATLAS, the CMS detector is relatively compact (14.6 m diameter and 21.6 m long).

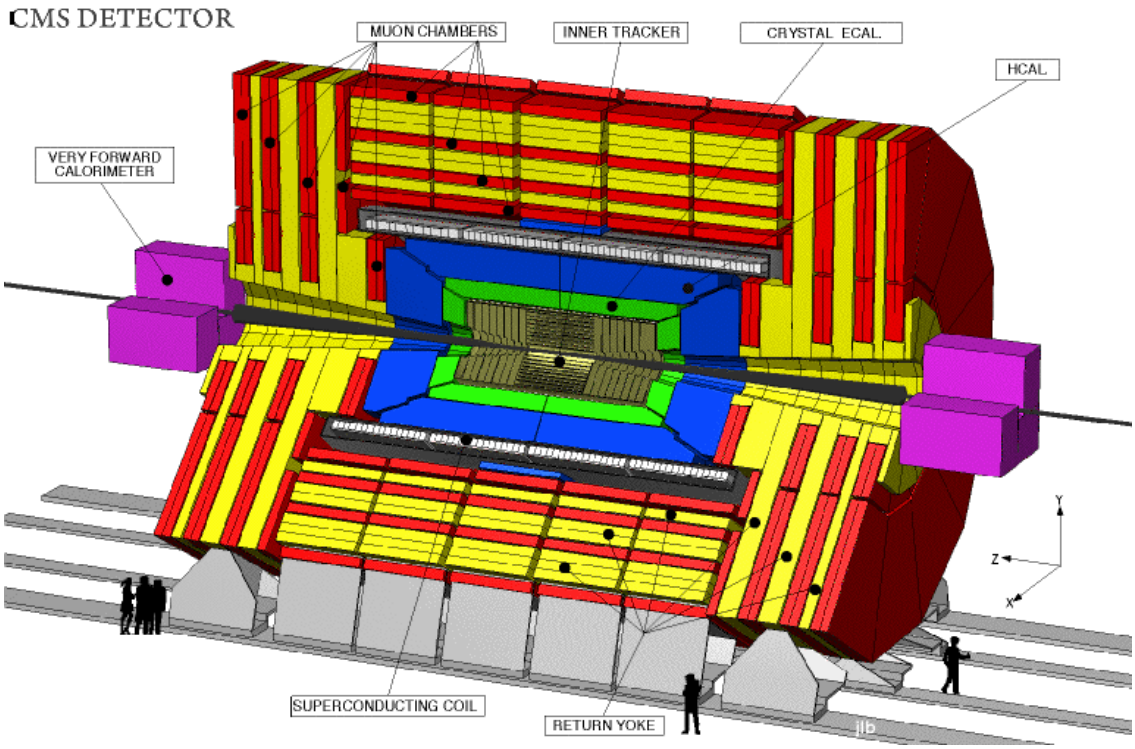


Figure 2.2: Illustration of the CMS detector, with the cartesian coordinate system as indicated.

The coordinate system used at the CMS experiment is defined by the z-axis, the azimuthal angle $\phi$ and the *pseudorapidity* $\eta$ defined as

$$\eta = -ln\left(tan\frac{\theta}{2}\right), \tag{2.4}$$

with $\theta$ the polar angle. The pseudorapidity is preferred as coordinate to the polar angle as it is invariant under Lorentz boosts along the z-axis. The origin of the coordinate system is located at the center of the CMS detector, which is considered as the nominal interaction point of the collisions. The detector is divided into three main parts; the barrel (central region) and two endcaps, enclosing the whole structure in order to detect the scattered particles up to a pseudorapidity of $|\eta| \leq 5.2$.

The functionality of all main subdetection systems is elaborated in the next sections, based on [28].

### 2.2.1 The inner tracker

The inner tracker measures interaction points from charged particles originating from a collision at several consecutive layers around the beam pipe. These points are combined into a track corresponding to an individual particle, using the *Kalman Filter* procedure [29]. The Kalman Filter procedure starts with an estimation of the track parameters and uncertainties from a *seed*, which is e hit in the detection layer closest to the beam pipe. With this estimation the track is extrapolated to the next detection layer, searching for compatible segments. Based on the compatible segment and the previous estimation, the track parameters are adjusted. This process is repeated until the final detection layer is reached. In this way the Kalman Filter takes all possible effects into account, such as multiple scattering, energy loss in material and non-uniform magnetic fields. The resulting track parameters represent a helicoidal trajectory, from which, knowing the magnetic field strength, the momentum of the particle can be determined.

The inner tracker consists of a silicon pixel detector and several layers of silicon strips, all connected to readout chips. The pixel detector is placed closest to the interaction point in order to precisely measure coordinates of decay vertices from particles which live long enough to escape the beam pipe. Consisting of 66 milion pixels, the pixel detector strives to obtain a high granularity and good spatial resolution. Each of the pixels is about 100 $\times$ 150 $\mu m^2$ large and the resolution is 10 $\mu$m in the (r $\times$ $\phi$) direction and 20 $\mu$m in the z-direction.

The silicon layers surround the pixel detector, with a total of 9.6 milion silicon strips. These layers are divided into subgroups, placed in different geometries to optimise the detection resolution. The structure of the inner tracker is schematically represented in Figure 2.3. In total the inner tracker is 5.4 m long, has a diameter of 2.4 m and measures tracks up to a pseudorapidity of $|\eta| = 2.5$.

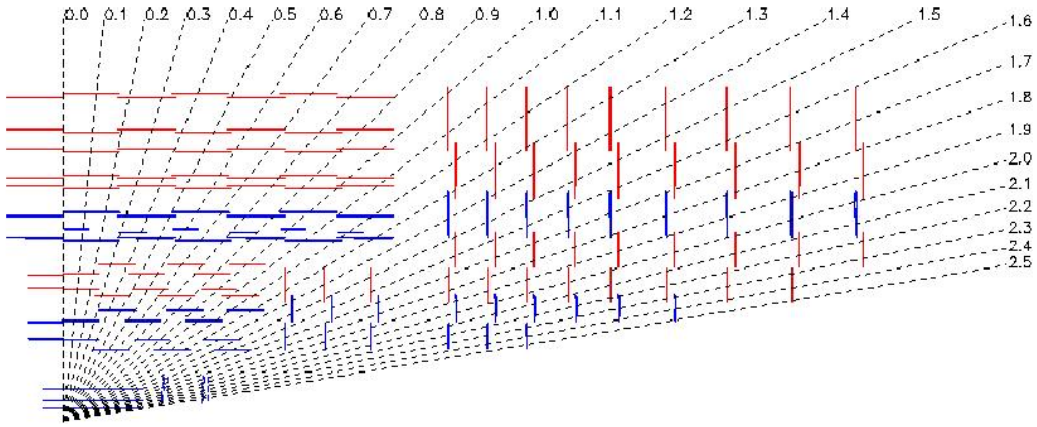


Figure 2.3: Quarter view on the inner tracker silicon strips and pixel detector.

### 2.2.2 Electromagnetic calorimeter

The electromagnetic calorimeters (ECAL) are designed to measure the energy of electrons and photons with a high resolution. Using 75 848 scintillating lead-tungstate ($PbWO_4$) crystals, the ECAL is optimised for the search in the two photon decay channel of the Higgs boson. Every crystal is connected to a photodiode to read out the scintillation light. $PbWO_4$ is a very fast scintillator, with 80% of the light signal being emitted within 25 ns. This enables the CMS ECAL to cope perfectly with sequential bunch crossings ($\sim$ 25 ns) at the intended luminosity of $10^{34}\text{cm}^{-2}\text{s}^{-1}$. A disadvantage of $PbWO_4$ is its low light yield.

The ECAL is divided into a barrel ECAL region (EB), covering $|\eta| < 1.48$, and an endcap ECAL region (EE), covering $|\eta| \in [1.48, 3]$, as shown in Figure 2.4. The crystals are 230 mm long and point towards the nominal interaction point, with a slight inclination ($\sim 3°$ in both $\phi$ as $\theta$ direction) in order to minimize the probability of a photon or electron to slip through two crystals undetected. The surface of a crystal, directed to the nominal interaction point, covers 1° in the $\phi$ and $\theta$ direction.

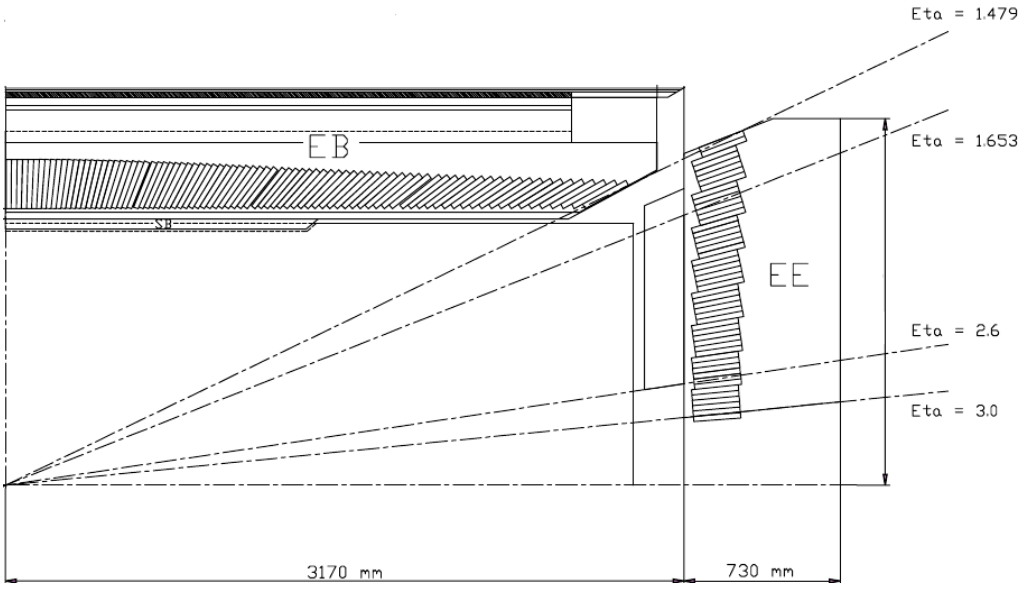


Figure 2.4: Quarter view on the CMS ECAL.

The energy resolution $\sigma$ of the CMS ECAL is parametrised as

$$\left(\frac{\sigma(E(GeV))}{E(GeV)}\right)^2 = \left(\frac{2.8\%}{\sqrt{E(GeV)}}\right)^2 + \left(\frac{0.12\%}{E(GeV)}\right)^2 + (0.30\%)^2, \qquad (2.5)$$

with E the energy of the particle. The first term represents the stochastic term, the second term is a noise term and the third term is a constant term.

### 2.2.3 Hadronic calorimeter

The hadronic calorimeters (HCAL) strives to measure the energy of hadrons. Unlike the ECAL, the HCAL is a sampling calorimeter, using alternating layers of absorbing material (brass) and scintillating tiles made of plastic as active material. The scintillation light from the tiles is guided by wavelength shifting fibres to hybrid photodiodes, which read out the scintillation light.

The HCAL system at CMS is divided into four pieces, according to their position in the detector: barrel HCAL (HB), endcap HCAL (HE), outer HCAL (HO) and forward HCAL (HF). This is schematically represented in Figure 2.5. The outer HCAL is implemented to measure the tails of hadronic showers making it to the outside of the solenoid. The HB covers $|\eta| < 1.4$, the HE $|\eta| \in [1.3, 3]$ and the HF covers up to $|\eta| < 5.2$. The forward HCAL is installed to make sure most of the energy dispersed in the transverse plane is accounted for, in order to get a good estimate of the transverse energy that escaped detection. Because the forward HCAL will be subject to a higher level of radiation, steel is used as absorbing material instead of brass and quartz fibres as active material. The quartz fibres will generate Cherenkov light and are more radiation hard than plastic.

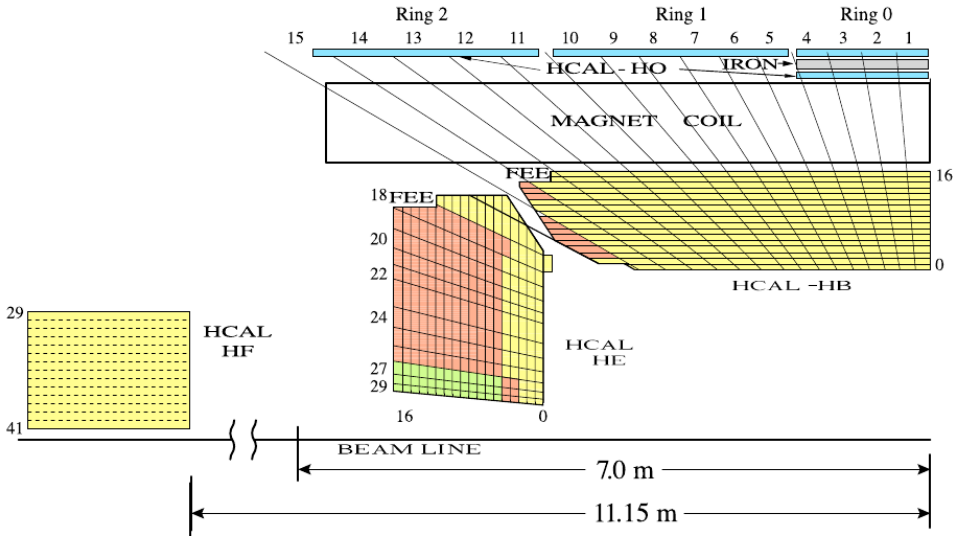


Figure 2.5: Quarter view on the CMS HCAL.

### 2.2.4 The muon detection system

Muons lose less energy to brehmsstrahlung than electrons due to their relatively large mass. This and their relatively large lifetime ($\tau_\mu \approx 2.2$ $\mu$s) amount to the fact that muons are hardly affected by the tracker, calorimeters and solenoid (or even other materials). Therefore muons will traverse the detector even outside the solenoid without being absorbed and leaving almost nothing but a charged trajectory. In order to identify muons originating from a collision, the CMS detector has a special muon detection system placed outside of the solenoid, embedded in the flux-returning yoke of the magnet.

The CMS muon detection system consists of several layers of Drift Tubes (DTs) in the barrel and Cathode Strip Chambers (CSCs) in the endcap, constructed inside the return yoke. The DTs and CSCs are gaseous detectors recording the passage of charged particles as segments with a high spatial resolution; 100 $\mu$m for the DTs and 200 $\mu$m for the CSCs. The angular resolution in the $\phi$-direction for the DTs is 1 mrad and 10 mrad for CSCs. DTs cover the region $|\eta| < 1.2$ and CSCs cover $|\eta| \in [0, 2.4]$. The real succes of the CMS muon detection system lies in the use of Resistive Plate Chambers (RPCs), which have a time resolution of 1 ns. Due to the excellent time resolution, the RPCs are able to associate detected muons to individual bunch crossings and are very important to the trigger system (see Subsection 2.2.5). RPCs are placed in both barrel as endcaps, always in combination with a DT or CSC, as shown in Figure 2.6.

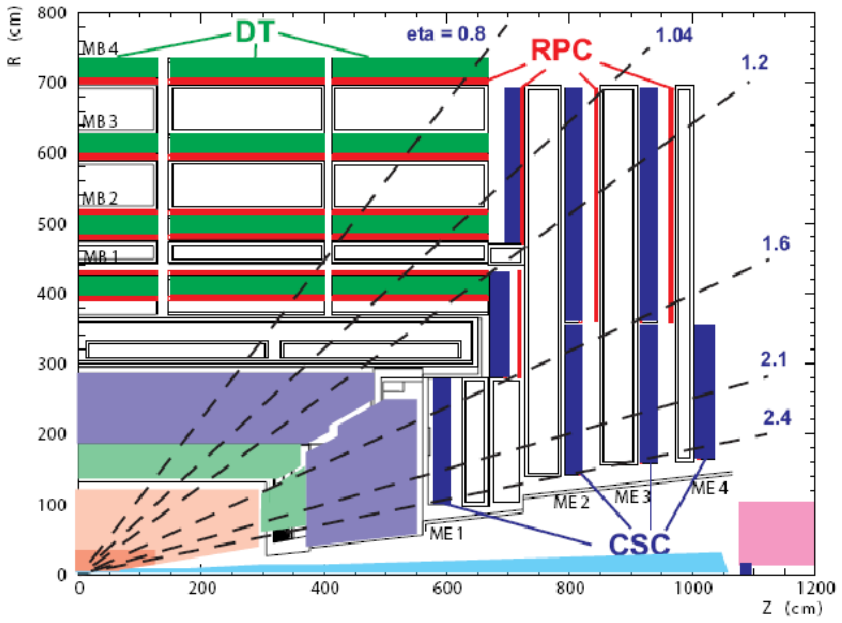


Figure 2.6: Quarter view of the CMS muon detection system. The non-coloured zones in the outer layers represent the return yoke of the magnet.

### 2.2.5 The trigger system

At the intended luminosity of $10^{34}\text{cm}^{-2}\text{s}^{-1}$, CMS has to deal with an event rate of the order of $10^9$ Hz, coming from bunches crossing over at a rate of 40 MHz. Every bunch crossing provides about 20 collisions, loading the detection system with a lot of information, of which most is not useful for further physics analysis, such as low energy hadronic processes and elastic collisions. As there is not enough data storage room for all events, online triggers are installed to reject uninteresting events before they are stored for physics analysis. CMS relies on two triggers to do this: the Level-1 (L1) trigger, a hardware trigger located at a control room near the detector, and a High Level Trigger (HLT), using computer farms at the surface to run the software.

The electronic signals from the detector are converted into digital information using digitizers. This raw data is sent to front-end pipelines, storing the information for 3.2 $\mu$s while L1 decides, based on fast algorithms, whether to keep the event or not. These algorithms need to be very fast and therefore only use information from the muon detection system and the calorimeters. The output rate after the L1 is reduced to the order of 100 kHz.

After the L1 has passed an event, the information of the event is read out by a buffer. Then the switching networks combine all the information from the subparts of the detector to reconstruct the event. The event information now contains reconstructed tracks and more detailed information from the calorimeters. The HLT uses this to make a more refined selection in the data in order to reduce the event rate to 100 Hz. These events are stored for offline analysis. The whole trigger process is schematically represented in Figure 2.7.

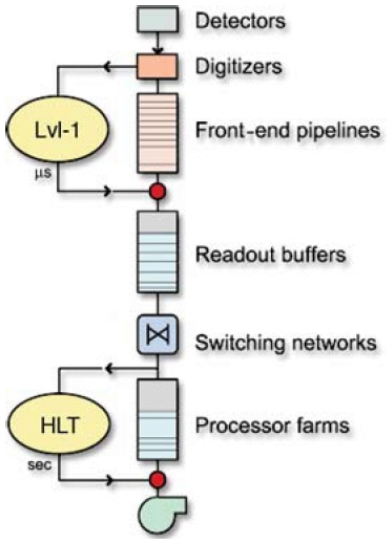


Figure 2.7: Schematic representation of the CMS trigger system.

# Chapter 3

# Event reconstruction and simulation

In order to analyse an event, the raw detector signals are interpreted in terms of energy and coordinates. With this raw information the detected hits are reconstructed in terms of physics objects, such as muons, photons... This chapter will discuss the reconstruction of physics objects relevant to this specific analysis, namely the reconstruction of jets, b-jets, muons and missing transverse energy. The software used to reconstruct physics objects is the *CMS Software Framwework* (CMSSW). More details on the reconstruction of these and other objects at the CMS experiment can be found in [28].

This analysis uses Monte-Carlo based simulations of SM phenomena, e.g. the production and decay of $t\bar{t}$, and the T1tttt process produced in proton collisions at the CMS experiment. The second part of this chapter discusses the several steps that are considered in these simulations at CMS, starting from the simulation of the hard process in the collision, to the fragmentation of partons and the final signature in the detector.

## 3.1 Particle flow event reconstruction

The method used at CMS to recunstruct and identify all stable particles in an event (e.g. photons, electrons, muons and hadrons) is called *Particle Flow* [30]. Particle Flow combines information from all CMS subdetectors to identify the particles and determine their direction and energy. In general the Particle Flow algorithm reconstructs particles one by one and removes the corresponding track(s) and energy deposit(s) in the HCAL and ECAL, before reconstructing the next particle in line. The algorithm starts with the particles that are less difficult to reconstruct and identify, to end up with the most difficult particles to identify. The considered hierarchy of reconstruction is first the muon, then the electron, photon and finally the charged and neutral hadrons. This ranking is based on the fact that the muon has a dedicated detector with the sole goal of identifying muons, hence making the muon the easiest to identify. Then the electron is easier to identify than the

photon as it leaves a track in the inner tracker, whereas the photon does not. The hadrons are the most difficult to identify compared to electrons and photons, as their energies are mostly deposited in the HCAL, which have a lower granularity and resolution than the ECAL.

The advantage of the PF approach is that the number of tracks and energy deposits decreases with every reconstructed particle as the algorithm progresses. This provides a better reconstruction of the hadrons than an all-together approach, where all particles are reconstructed simultaneously.

### 3.1.1 Muon reconstruction

Muon reconstruction starts with a *standalone* reconstruction from hit segments in the muon detection system. The standalone reconstruction builds the track of a L1 triggered muon using the Kalman Filter technique (see Subsection 2.2.1) in the outer layers of the detector. The hit used as seed in this procedure is a segment as detected in the first layer of CSC and DT muon chambers (also RPC hits are used as auxiliary information).

The second step is the *global* reconstruction of the muon, where the information from the inner tracker is used in conjunction with the standalone reconstruction. The track parameters obtained from the standalone reconstruction are used to define a region of interest in the inner tracker. In that region of interest a track is reconstructed following the Kalman Filter procedure and is fitted to the standalone reconstructed track. The resulting track from the combined inner tracker and muon detection system defines the muon track.

Knowing the momentum p of the muon, from the track reconstruction, and its rest-mass $m_0 = 105.7$ MeV/c$^2$ [31], the energy of the muon can be calculated using the relativistic identity $E^2 = p^2c^2 + m_0^2c^4$.

### 3.1.2 Jets

Due to colour confinement (see Section 1.1.2) individual partons will never be detected as such. They will branch into other partons and fragment to form hadrons, which produce a shower of secondary particles in the HCAL detector. The process of parton showering and fragmentation is a complicated process, which is described by QCD Perturbation Theory [32]. However hadrons and secondary particles coming from a parton showering and fragmentation, are mostly destined to end up in the same angular region of the detector. By means of an algorithm, such particles can be grouped into a *jet*, which can be interpreted as a representative of the original parton. A detailed study of several jet algorithms is given in [33].

The jet finding algorithm used in the CMSSW is the *Seedles Infrared Safe Cone* (SIScone) algorithm. The SIScone algorithm measures the difference $\Delta R_{ij}$ between particles labeled 'i' and 'j' as

$$\Delta R_{ij} = \sqrt{(\eta_i - \eta_j)^2 + (\phi_i - \phi_j)^2}, \tag{3.1}$$

for all particles. Then it iteratively clusters particles for which $\Delta R_{ij}$ is smaller than a pre-defined radius R into cones. Once particles are clustered into cones, this cone

is called a proto-jet. The four momentum of the proto-jet is defined by adding the four-momenta of its constituents. If the direction of the proto-jet is the same as that of the clustered constituents, the cone is called stable. If not, the algorithm is repeated by building a new cone around the direction of the clustered constituents until a stable cone is found. If all particles in an event are combined into stable cones, the algorithm stops and the jets are formed as these stable cones.

### 3.1.3 b-jet identification

While jet finding algorithms are designed in order to represent the original parton as a physics object, it is practically impossible to determine what type of parton the jet originates from. However the decay properties of a b-quark provide observable signatures, which are distinguishible from the decay signatures of other quarks, making it possible to tag a jet as b-jet. The two main observables which discriminate b-parton-like behaviour versus light-parton-like behaviour are:

- *Impact parameter* ($IP$): An observable which is found to be discriminating in b-tagging, is the impact parameter (IP), defined as the distance between the primary vertex and the extrapolated track at the point of closest approach, as schematically represented in Figure 3.1. The IP is calculated for all tracks closer than $\Delta R = 0.5$ (3.1) to the jet axis. A more refined use of the IP is the IP significance which takes the resolution on the IP into account as $\text{IP}_{sign} = \frac{IP}{\sigma_{IP}}$, with $\sigma_{IP}$ the resolution on the IP. In b-tagging the IP significance is used instead of IP.

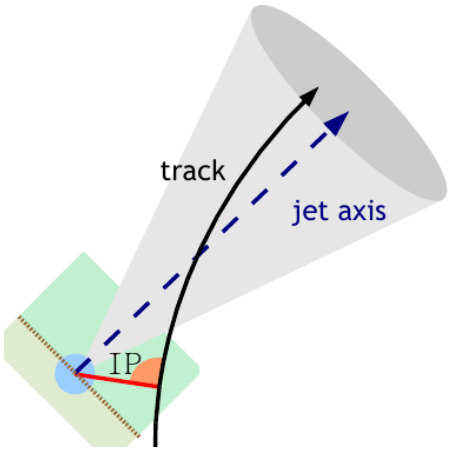


Figure 3.1: Illustration of the impact parameter between a track and the primary vertex.

- *Secondary vertex*: Due to its relatively large mass[1] the b-quark fragmentation can contain heavy B hadrons, which have a relatively long lifetime. Thereby the B hadron will travel an observable distance in the detector before decaying,

[1] Even though the t-quark is heavier, it can not be identified with individual jets due to the fact it practically does not hadronize, but mainly decays to other elementary particles.

producing a displaced secondary vertex which is experimentally distinguishible from the primary vertex.

The b-tagging procedure used in this analysis is complex, called the *Combined Secondary Vertex* algorithm (CSV) [34], and mainly combines the secondary vertex information with the track impact parameter significances to build a variable which is able to discriminate b-parton jets from light jets. Three different requirements can be made on b-tagging: Loose (L), Medium (M) or Tight (T) b-tagging, rendering a misidentification probability for light jets as b-jets of respectively around 10%, 1% and 0.1%. A jet passes a requirement when its CSV discriminator value is bigger than the required value. An offline performance of the CSV algorithm [34] is given in Figure 3.2, based on a sample of simulated QCD jets.

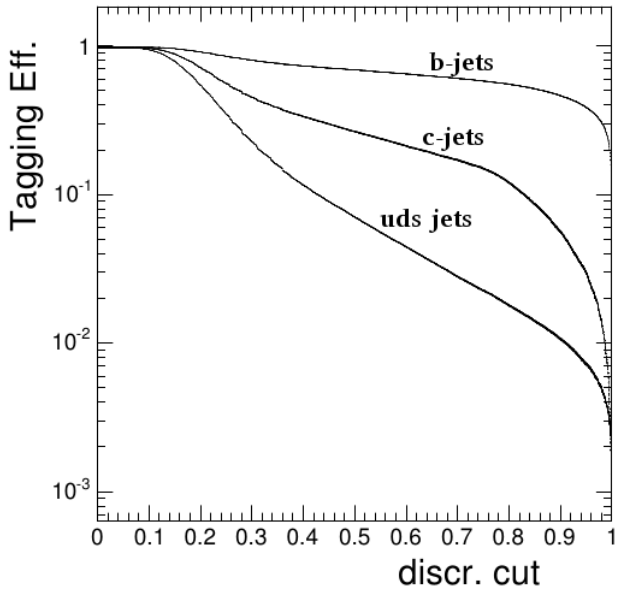


Figure 3.2: Efficiencies to tag a jet as b-jet, as a function of the CSV discriminator value for b-jets (top curve), c-jets (middle curve) and light jets (bottom curve), based on simulated events, as taken from [34].

In this analysis the Medium b-tagging requirement is applied, which requires jets to have a CSV discriminator value $\geq 0.679$. Typically the efficiency to b-tag a b-parton jet is about 60 % and the efficiency to b-tag a ligh-parton jet is about 2%[2].

### 3.1.4 Missing transverse energy

Even though the detector has a high granularity and good hermiticity, the energy of an event will never be completely reconstructed. A great deal of the energy is directed in the very forward region and disappears down the beampipe. The energy dispersed in the plane transverse to the beam pipe however, can be measured quite

[2] The b-tagging effeciency differs for data and simulations, so the values quoted here are no absolute b-tagging efficiencies.

accurately. Knowing the transverse momentum of the proton-proton system is zero, one can determine the *missing transverse energy* (MET) [35] by measuring the transverse energy balance in an event as defined by the calorimeter towers. These calorimeter towers are constructed by adding the energy contributions from the ECAL and HCAL, as shown in Figure 3.3.

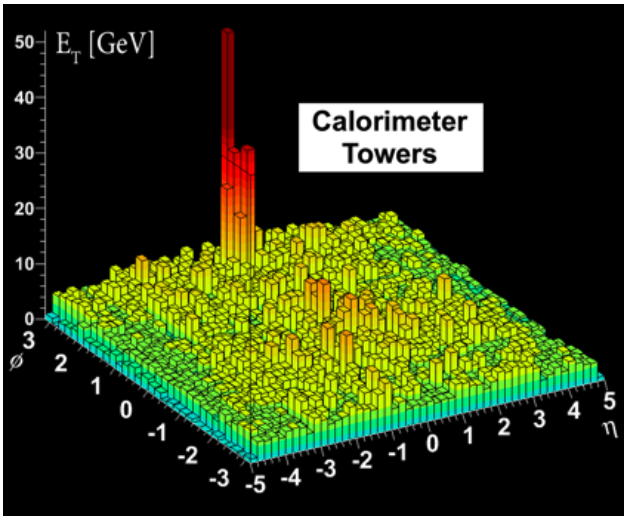


Figure 3.3: Visualisation of the energies in calorimeter towers in the ($\eta$,$\phi$) plane, as taken from [3].

The missing transverse energy is a good representative of weakly interacting stable particles which escape detection, such as neutrinos or the unknown WIMPs. The vector of the MET is calculated by vectorially summing the energy contributions $E_n$ of all individual calorimeter towers, with coordinates $\eta_n$ and $\phi_n$

$$\vec{E}_T^{miss} = -\sum_n E_n \left( \frac{cos\phi_n}{cosh\eta_n} \vec{1}_x + \frac{sin\phi_n}{cosh\eta_n} \vec{1}_y \right), \tag{3.2}$$

where the minus sign is a convention.

One must take care for the misinterpretation of MET as always being the consequence of genuine particles escaping detection. MET is often due to detector effects, such as limited detector range, detector granularity, electronic noise, energy resolution of the calorimeters, pile up of detector signals due to sequential collisions, energy tresholds... All these effects worsen the MET even more if an event has a large total activity, which can be quantified as the total scalar transverse energy $\sum E_T$, defined as the scalar sum of all calorimeter towers. The resolution $\sigma$ on the MET has been modeled as [35]

$$\sigma^2 \approx (3.8GeV)^2 + (0.97GeV^{1/2}\sqrt{\sum E_T})^2 + (0.012 \sum E_T)^2. \tag{3.3}$$

This results in a resolution of 45 GeV in an event with a reconstructed transverse momentum of 800 GeV/c.

## 3.2 Event simulation

Every model analysis is based on a comparison between the measured data and a prediction for that model. In this analysis the prediction for the models (SM and T1tttt processes) are Monte-Carlo (MC) simulated. The MC simulation of collisions of two protons and the resulting final state can be considered in two steps. The first step consists of getting two partons out of each proton and describing their interaction to the hard process of interest. The second step is simulating the partons decaying into other partons, including those not taking part in the hard process. This step also involves the fragmentation of partons due to colour confinement. In order to compare the MC samples with the measured data, detector effects and additional factors need to be taken into account.

### 3.2.1 Proton collisions at a fundamental level

#### Hadronic cross section

The theoretical calculation of the cross section of a proton-proton collision to a final state $X$, denoted as $\sigma_{pp\to X}$, can be formulated [36] as the convolution of the 'partonic' cross section[3] ($\hat{\sigma}_{ab\to X}$) and the parton distribution functions (PDFs) of the protons' partons

$$\sigma_{pp\to X} = \sum_{a,b} \int_0^1 dx_1 \int_0^1 dx_2 f_a(x_1, Q^2) f_b(x_1, Q^2) \hat{\sigma}_{ab\to X}(x_1, x_2, g_3(Q^2)), \tag{3.4}$$

with $f_a$ and $f_b$ the PDFs for the two protons, $x_1$ and $x_2$ the momentum fractions the considered partons take from the proton, $Q^2$ the energy scale at which the interaction is considered and $g_3$ the strong coupling constant. The sum is considered for all possible parton flavours, spins, ...

The differential partonic cross section is given by

$$d\hat{\sigma}_{ab\to X} = \frac{|\mathcal{M}|^2}{64\pi^2 s_{real}} dcos\theta d\phi, \tag{3.5}$$

with $s_{real}$ as defined in (2.3) and $\mathcal{M}$ the matrix element of the process, which can be calculated with the Feynman rules. The software used for the calculation of the matrix elements is in these simulations is MadGraph [37]. The dependence of $\hat{\sigma}_{ab\to X}$ to the strong coupling constant $g_3$ is provided in the matrix element. Mostly the matrix element is only calculated for a fixed number of final state partons at Leading Order (LO) and virtual loops in the Feynman diagrams are not considered. In order to take Next to Leading Order (NLO) processes into account, the K-factor is introduced, representing the relative strength of the NLO cross section to the LO cross section

$$K = \frac{\sigma_{NLO}}{\sigma_{LO}}. \tag{3.6}$$

[3] This refers to the cross section which produces the final state $X$ from partons a and b

The K-factor depends on the region of phase-space $(\eta, \phi)$ and on the PDFs used for the LO and NLO calculations.

The PDFs are experimentally determined quantities evaluated at a certain $Q^2$ value. The extrapolation of the PDFs to higher interaction scales is provided by the DGLAP equations [38–40]. An example of the PDFs at $Q^2 = 10$ GeV for a proton is given in Figure 3.4.

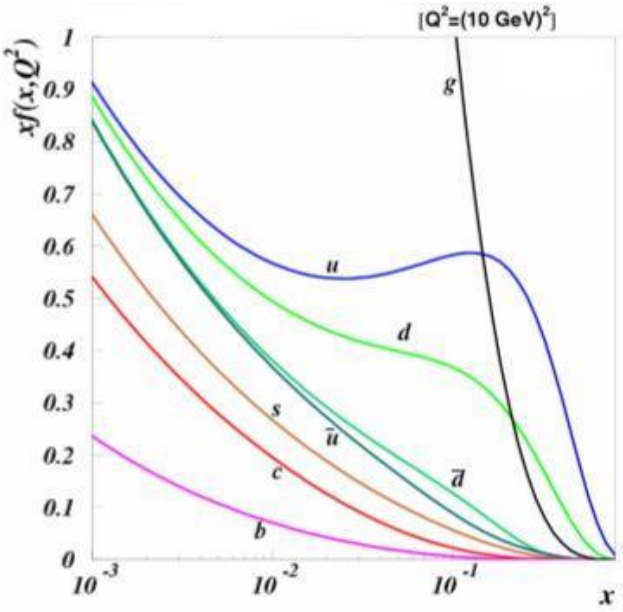


Figure 3.4: Parton distribution functions for the dominating parton flavours in a proton considered at $Q^2 = 10$ GeV.

It is important to note that the calculation of the total hadronic cross section for a final state $X$ is in general considered with respect to two main energy scales, to which $Q^2$ is sized: the *factorization scale* ($\mu_F$) and the *renormalisation scale* ($\mu_R$) [41]. The factorization scale is a measure for the scale at which perturbation theory is no longer trusted. The untrustworthy aspect of perturbation theory comes from the soft and collinear divergences, which correspond to a long-range part of the strong interaction. The renormalisation scale is introduced to regulate the UV cutoff in order to get rid off divergences in internal loops.

A change in both scales will affect the PDFs, partonic cross sections, K-factors and will non-trivially alter the resulting cross section and kinematics. As these scales are not explicitly defined by theory, they can adopt different values. Usually these scales are fixed to the energy scale of the interaction under study, so the nominal MC samples are created by considering them at the interaction energy scale ($\mu_F = \mu_R = Q^2$). On the other hand, to estimate the full range of uncertainty on the interaction scale, samples are created where $\mu_F$ and $\mu_R$ are varied simultaneously and independently in the range $0.5Q^2 \leq \mu_F,\mu_R \leq 2Q^2$ with the constraint $0.5 \leq \mu_F/\mu_R \leq 2$. The systematic uncertainty is then taken to be the maximum deviation resulting from this scale variation and will be referred to as *scaling*.

#### Parton evolution

When individual partons emerge from the hard collision, they will decay into other partons producing a shower of secondary partons. This radiation is controlled by the strong coupling constant, which strongly depends on the energy scale of the interaction. The parton showering is handled in the second stage of collision simulation, where the parton showers are simulated seperately from the individual partons. These showers are combined by a jet finding algorithm to construct a jet.Every parton, starting with the highest $P_T$ parton, is matched to the nearest jet for which $\Delta R$ between parton and jet is smaller than $R_{jet}$. If each parton has a matched jet, the event is fully reconstructed, if not the event is rejected. Depending on the matching parameters $R_{jet}$ and $E_{jet}$, the number of MC simulated events, number of jets and kinematics of the process will alter. The appropriate values of the matching parameters are not precisely known, therefore there is a systematic uncertainty associated with the imprecise knowledge of this parameter. This type of systematic uncertainty will be referred to as *matching*.

Afterwards the parton showers are fragmented according to string fragmentation models [9]. Also the evolution of partons not taking part in the hard collision (i.e. the remains of the proton) is simulated. The software that takes care of the parton showering and fragmentation is PYTHIA [42]. This is referred to as the *underlying event*.

### 3.2.2 Detector simulation

The final step of the event simulation is performed by the CMSSW simulation procedure, which simulates the detection of particles via the GEANT4 software [43]. From the detection simulation the object reconstruction is performed by CMSSW as described in Section 3.1.

All samples (including data) are stored in $TopTree$ datasets for further analysis, which are lighter versions of the full samples. These TopTrees are analysed and compared in the ROOT platform [44]. Full TopTrees aren't always a necessity, so in order to reduce CPU time TopTrees can be sized down by pre-selecting certain events. This pre-selection is referred to as *skimming*.

### 3.2.3 Corrections

There are several factors which need to be taken into account to correct the behaviour of MC samples compared to data. The most significant corrections are for $Pile-Up$ (PU), $Jet\ Energy\ Corrections$ (JEC) and $b-tagging\ efficiencies$. These corrections are applied after the MC samples have been created. Corrections such as these depend on the data and have significant uncertainty, which will have to be taken into account later on in the analysis as systematic uncertainties.

### Pile – Up

Pile-up occurs when the readout of the detector includes information from more than one proton collision. There are mainly two types of pile-up at the CMS experiment: in-time pile-up, due to additional collisions in the same bunch crossing, and out-of-time pile-up, due to residuals from collisions of previous bunch crossings. The amount of pile-up in simulation is different from the one observed in data. Therefore a reweighting is applied to simulation in order to bring the data and simulation distributions into agreement.

### Jet Energy Corrections

It is not straightforward to connect the energy of the true parton to its corresponding jet energy. This is due to the fact that the calorimeter response to particles is not straightforward.Therefore, the jet energies in simulations need to be corrected for this nonlinear behaviour. In order to correct for misconstructed jet energies in simulations, CMS offers a factorized approach [45], where in different steps the nonlinear energy response is modelled and corrected for. The different levels are applied sequentially, with the output of each step being the input of the next. At every level of the JEC, the jet four momentum is scaled with a factor, which depends on various jet related quantities, such as pseudorapidity, flavour, etc. In this analysis JEC are considered in three levels:

- Level 1: Energy coming from pile-up events is removed.
- Level 2: $\eta$ dependences are eliminated from the jet response.
- Level 3: $P_T$ dependences are removed from the jet response.

These corrections will alter the kinematics of the final state, rendering a systematic effect on the analysis.

### b – tagging efficiencies

The b-tagging efficiency is different between data and simulation. The b-tagging efficiencies are calculated as

$$\epsilon = \frac{N_{tag}}{N_{true}}, \tag{3.7}$$

with $N_{tag}$ the number of b-tagged jets and $N_{true}$ the number of true b-jets. In MC $N_{true}$ is easy to determine as a parton flavour is connected to every jet from the generation level. In data $N_{true}$ is determined in a b-enriched control sample as for example in [46].

When using b-tagged jets in an analysis it is very important to take this difference between data and simulation into account by means of scale factors

$$SF = \frac{\epsilon_{data}}{\epsilon_{MC}}. \tag{3.8}$$

These scale factors depend on the flavour, $P_T$ and pseudorapidity of the jets. From here on two different approaches exist to correct the MC samples for b-tagging efficiencies: an approach that reweights MC events according to the b-tagging scale factors [47] and an approach in which the b-tagged status of a jet is updated jet by jet [48]. In this analysis the second approach is used.

The jet-by-jet updating upgrades (or downgrades) the b-tagged status of every jet according to the scale factor. If the b-tagging efficiency is higher in MC than in data (SF $< 1$), a fraction (1-SF) of the b-tagged jets in the MC event is downgraded to non-b-tagged jets, such that $\epsilon_{data} = \epsilon_{MC}^{updated}$. If on the other hand the b-tagging efficiency in data is higher (SF $> 1$), a fraction f of the non-b-tagged jets' status is upgraded to b-tagged jets, where f is defined as

$$f = \frac{1 - SF}{1 - \frac{1}{\epsilon_{MC}}}. \tag{3.9}$$

This equation is a straightforward deduction from the desire to have $\epsilon_{data} = \epsilon_{MC}^{updated}$. In order to achieve this $\epsilon_{MC}^{updated}$ is easily obtained by $\epsilon_{MC}^{updated} = \epsilon_{MC} + f(1 - \epsilon_{MC})$. Great care has to be taken when using this approach if SF $> 1$, because this way of upgrading/downgrading the b-tagged status of a jet adds a totally random component to the collection of b-tagged and untagged jets. This random aspect of this method leads to the fact that b-tag related variables become ill-defined In order to avoid such variables in this analysis the b-tagging tool will only be used to select on a number of b-tagged jets and variables relying on b-tagging properties will be avoided. A similar procedure is set up to account for mistagging light jets as b-tagged jets.

# Chapter 4

# Experimental analysis of T1tttt process

In this chapter the procedure in which the T1tttt process is differentiated from SM background processes, is presented.

The T1tttt channel has many different final state configurations, based on the number of leptons, their charge and flavour. Numerous SM processes, such as the production of $t\bar{t}$, Z bosons, W bosons and dibosons VV (WW, WZ and ZZ) can produce similar signatures to T1tttt. In order to suppress these as much as possible, broad selections will be made in the final state channel, based on the number of jets, b-tagged jets and amount of MET. After suppressing the background with these selections, the kinematic properties of the simulated signal and background will be studied to find a set of variables which are more sensitive to signal-like processes compared to the background. These variables are combined into a multivariate analysis to produce a likelihood ratio discriminator, which will be used in Chapter 5 to calculate an upper limit on the considered T1tttt process. The data set used for this analysis, was recorded at CMS in 2012 with an integrated luminosity of 18.83 $\text{fb}^{-1}$.

## 4.1 Choice of final state

All possible final states of a topology with four top quarks will be given, classified according to the number of leptons, their charge and flavour. By means of the branching ratios for the involved particles to decay into secondary particles, an estimate is given for the number of expected events for both signal and background in every final state. The considered SM background processes are: $t\bar{t}$ + jets, Z + jets, W + jets, VV (WW, WZ and ZZ), single top quarks + jets (all channels), $t\bar{t}$ + single boson $t\bar{t}$V ($t\bar{t}$Z and $t\bar{t}$W). These processes are listed in Table 4.1 with their respective cross sections as taken from [49].

Table 4.1: List of all considered SM background processes relevant to this analysis with their respective total cross sections at $\sqrt{s} = 8$ TeV.

| Process | Cross section |
|---|---|
| $t\bar{t}$ + jets | 225.197 pb (NLO) |
| Z + jets | 3503.7 pb (NNLO) |
| W + jets | 36257.2 pb (NNLO) |
| SingleTop + jets (all channels) | 114.15 pb (NNLO) |
| WW + jets | 56.75 pb (NLO) |
| WZ + jets | 33.8 pb (NLO) |
| ZZ + jets | 8.059 pb (NLO) |
| $t\bar{t}$W + jets | 0.215 pb (NLO) |
| $t\bar{t}$Z | 0.172 pb (NLO) |

### 4.1.1 Final states of the four top quark topology

All masses, lifetimes and branching ratios cited in this subsection are taken from [31].

There are mainly two ways in which prompt charged leptons can be produced: a W boson decaying into a charged lepton + neutrino ($W \to l\nu$) and Z decaying into two charged leptons ($Z \to ll$). The corresponding approximate branching ratios for the decays of Z and W bosons are given as

$$BR(W \to q\bar{q}) \approx \frac{2}{3}, \tag{4.1}$$

$$BR(W \to l\nu) \approx \frac{1}{3}, \tag{4.2}$$

$$BR(Z \to q\bar{q}) + BR(Z \to \nu\bar{\nu}) \approx \frac{9}{10}, \tag{4.3}$$

$$BR(Z \to l^+l^-) \approx \frac{1}{10}. \tag{4.4}$$

The top quark has a very short lifetime ($\tau_t \approx 5 \times 10^{-24}$s) due to its high mass ($m_t = 173.5 \pm 0.6 \pm 0.8$ GeV/c$^2$). Because it is so short-lived, the top quark will decay to lighter particles before it hadronizes[1]. The CKM matrix indicates that in almost 99.9% of the cases the top quark decays to a b-quark and a W boson ($t \to bW$), where the b-quark hadronizes and is reconsutructed as a jet and the W boson decays as portrayed above.

With these estimations of the branching ratios of the top quark, W boson and Z boson, an estimate will be given of the number of signal (S) and background (B) events in a data set with an integrated luminosity of 20 fb$^{-1}$, for every possible final state in the four top quark channel. The SM cross sections are taken from Table 4.1 and the cross section used to calculate the number of signal events is 25 fb. The estimation is given in Table 4.2, together with a significance of the signal for the given leptonic final state, defined as $S/\sqrt{B}$, which gives the number of Poissonian

[1] The top quark decays ∼20 times faster than the strong interaction timescale.

standard deviations the signal is expected to differ from the background. This means that any number of signal events that could be accomodated for by the uncertainty on the background, is not significant enough to be discovered (as is the case for all channels listed in Table 4.2). The most ideal significance for the discovery (or exclusion) of signal, is five standard deviations (or a significance of five). The final state with the highest significance will be the most sensitive channel to look for signal. It is important to note that this significance is just a preliminary estimation, as the uncertainty on the background is just considered as a Poissonian uncertainty instead of the uncertainty coming from systematic variations on the background.

The number of estimated background events for each channel is given only for the two main background processes. Note also that single Z boson production is not included. It is assumed that Z events can be easily removed by applying a requirement on the MET, hence they are not expected to be a significant background (see further Subsection 4.1.3). Tau leptons are not included in these calculations as well, because they rapidly decay into other leptons or even quarks, which makes the tau leptons hard to reconstruct. For the exclusion of the tau lepton, the probability for every lepton flavour is assumes equal, namely 1/3.

Table 4.2: Estimation of the number of expected signal (S) and background events (B) for all possible leptonic final states for an integrated luminosity of 20 fb$^{-1}$. Tau leptons are excluded, as are Z boson productions. The significance of the signal for every final state is given as $S/\sqrt{B}$. The charges of the leptons are indicated as $\pm$ and the subscripts a and b represent the possible lepton flavours 'electron' and 'muon', with a $\neq$ b.

| lepton charge$_{flavour}$ | S | B | $S/\sqrt{B}$ |
|---|---|---|---|
| 0 | 99 | 483429333 + 889667 (W & $t\bar{t}$) | 0.0045 |
| $\pm_a$ | 132 | 161143111 + 1334500 (W & $t\bar{t}$) | 0.0103 |
| $+_a$ $-_a$ | 11 | 111208 + 21930 ($t\bar{t}$ & tW) | 0.0301 |
| $+_a$ $-_b$ | 11 | 111208 + 21930 ($t\bar{t}$ & tW) | 0.0301 |
| $\pm_a$ $\pm_a$ | 5 | 318 ($t\bar{t}$W) | 0.2804 |
| $\pm_a$ $\pm_b$ | 5 | 318 ($t\bar{t}$W) | 0.2804 |
| $\pm_a$ $\mp_a$ $\mp_a$ | 1 | 14 + 433 ($t\bar{t}$W & WZ) | 0.0473 |
| $\pm_a$ $\mp_b$ $\mp_b$ | 1 | 14 ($t\bar{t}$W) | 0.2673 |
| $\pm_a$ $\mp_a$ $\mp_b$ | 1 | 14 + 433 ($t\bar{t}$W & WZ) | 0.0473 |
| + + - - (all flavours) | 1 | 1612 (ZZ) | 0.025 |

In this analysis the opposite-sign (OS) dimuon channel will be investigated for T1tttt, meaning the final state of the signal process is

$$\tilde{g}\tilde{g} \rightarrow (t\bar{t}\tilde{\chi}_1^0)(t\bar{t}\tilde{\chi}_1^0) \rightarrow (b\mu^+\nu\bar{b}q\bar{q}\tilde{\chi}_1^0)(\bar{b}\mu^-\bar{\nu}bq\bar{q}\tilde{\chi}_1^0),$$

which roughly leads to an estimated signifcance of $S/\sqrt{B} = 0.0212$. The considered LO process creates eight partons, of which four are b-quarks, two OS muons and a large amount of MET due to two neutralinos and neutrinos.

Although the same sign (SS) dilepton and three lepton channels give better significances, the OS dilepton channel is chosen first, but extra sensitivity is expected if the analysis is combined with the other OS and SS dilepton channels. This choice is also based on the fact that in the OS channel real processes will dominate the background instead of fake backgrounds, which are due to the charge misidentification of leptons in the detector or the misidentification of a non-prompt lepton as prompt. The difficulty in simulating such fake backgrounds makes the SS and three lepton channels unsuitable for inclusion in a multivariate analysis. Muons were chosen, because they are better reconstructed than electrons.

### 4.1.2 Other T1tttt searches

Several of the final state topologies listed in Table 4.2 are being experimentally searched for the T1tttt channel (and other SMS topologies as well) at the LHC experiments. For example, in [50, 51] searches for the full hadronic final state of T1tttt are presented, in [52] the final state with one lepton is investigated, in [53] a SS dileptonic search is performed and in [54] the multilepton channel (three or more leptons) is used in the search for SUSY. These searches have excluded T1tttt processes for a certain range of masses of the gluino and LSP as shown in Figure 4.1. The upper part of the mass region is excluded, because that's the region where $m_{LSP} > m_{gluino}$ - 2 $m_t$, which is kinematically not allowed ($\tilde{g} \rightarrow t\bar{t}\tilde{\chi}_1^0$). So far

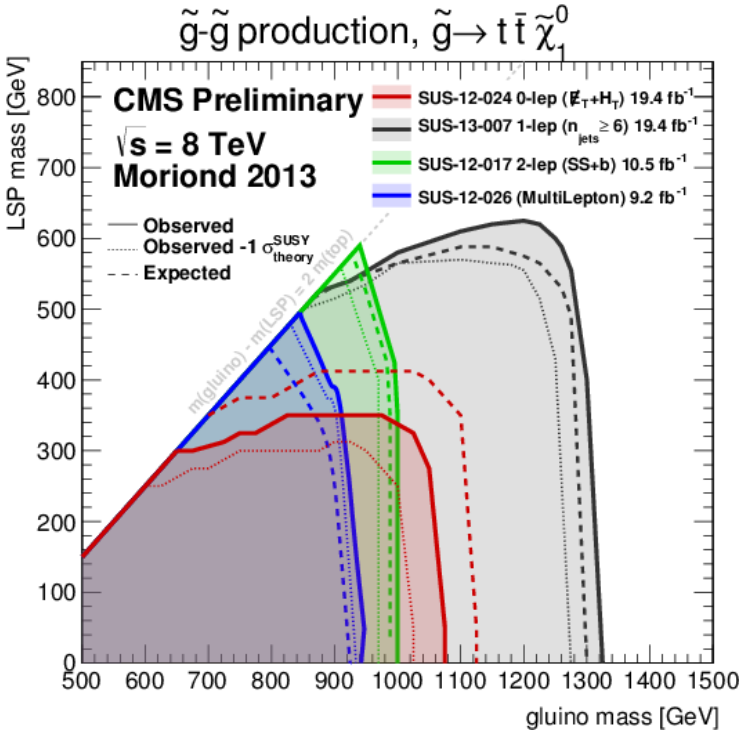


Figure 4.1: Preliminary results on the exclusion of certain values of $m_{gluino}$ and $m_{LSP}$ with a confidence level of 95%, based on the analyses mentioned in the text.

no analysis has presented results on the T1tttt search in the OS dilepton channel,

which means this analysis is complementary to those mentiond above.

This analysis will focus on one specific point in the unexcluded parameter space in Figure 4.1: $m_{\tilde{g}} = 1050$ GeV/c$^2$ and $m_{\tilde{\chi}_1^0} = 650$ GeV/c$^2$, with a a cross section of 25 fb at $\sqrt{s} = 8$ TeV. This mass point is a part of the *compressed spectrum* [55], meaning the mass ratio $m_{LSP}/m_{\tilde{g}}$ is significantly smaller than the prediction of mSUGRA ($m_{LSP}/m_{\tilde{g}} \approx 1/6$). In a compressed mass spectrum the decay channel $\tilde{t} \to q\bar{q}\chi_1^0$ is severely suppressed at collider experiments, due to phase space suppression of decay modes with heavy particles. As most light stop searches heavily depend on this decay channel, its suppression would provide a satisfactory explanation for the lack of experimental indications for the light stop quark so far[2]. The MET in compressed spectra is also typically lower than in compressed spectra, making searches which heavily depend on MET-related variables less sensitive to the compressed spectrum. The lower MET is due to the fact that most of the energy in the decay of the gluino goes into the mass of the neutralino.This results in a lower kinetic energy of the undetected neutralino, meaning the MET will be smaller.

In order to cope with the decreased sensitivity of MET-related variables in compressed spectrum searches, additional kinematic variables will be considered to approach the same performance (see further, Section 4.2).

### 4.1.3 Baseline selection criteria

In order to reduce the number of background events while preserving high efficiency on signal events, the topological and kinematic properties of signal are exploited. The signal is expected to produce eight jets of which four are b-tagged, whereas most of the considered SM backgrounds produce less jets, e.g. WW is expected to produce no jets at LO, $t\bar{t}$W is expected to produce two jets of which one is b-tagged. By requiring at least five jets, of which two are b-tagged, next to the OS di-muon requirement, such processes are greatly reduced to a level at which they are comparable to the number of signal events. Table 4.3 lists the effect of these requirements on the data and simulated samples. Note that the requirement of exactly two muons also holds a veto on electrons and these numbers still are a preliminary estimation, where no systematic effects are taken in to account. The first three jets in the selection are required to have a $P_T \geq 30$ GeV/c and the other two jets at least $P_T \geq 20$ GeV/c. The requirement on the transverse momenta of the first three jets is a consequence of skimming (see Section 3.2), whereas the requirement on the transverse momenta of the remaining two jets, is a direct requirement of the detector.

Table 4.3: Selection table summarising the effects of the baseline selection on the number of events for simulation and data for 18.8 $fb^{-1}$ of integrated luminosity.

| | *T1TTTT* | *W + jets* | *SingleTop + jets* | *VV* | *ttV* | *tt̄ + jets* | *Z + jets* | $S/\sqrt{B}$ |
|---|---|---|---|---|---|---|---|---|
| exactly 2 isolated OS muons | 4.1 | 9.8 | 654.2 | 1928.7 | 96.6 | 13560.0 | 112341.6 | 0.01143 |
| $\geq$ 5 jets, $\geq$ 2 bTags | 2.6 | 0.0 | 18.3 | 10.7 | 22.1 | 990.2 | 581.3 | 0.06455 |

[2] As explained in Chapter 1 the mass of the stop quark should be lighter than about 1 TeV, which is well within the detection range of the CMS and ATLAS experiments.

After this baseline selection, two backgrounds remain dominant over the signal: $t\bar{t}$ + jets (990.2 events) and Z + jets (581.3 events). The number of expected signal events is 2.6. The significance of the signal is increased with a factor of roughly six from 0.01143 (exactly two OS muons) to 0.06455 (exactly two OS muons + at least five jets of which 2 are b-tagged).

### Data to MC agreement

Since the analysis is based on simulations, it is important to ensure that the MC simulated events agree with the measured data events from the CMS experiment, within the scope of the systematic uncertainties on simulations. If the agreement is bad, the simulations can not be trusted upon for further analysis. The data to MC agreement is checked for the baseline selection of exactly two OS muons, at least 5 jets of which two are b-tagged.

Looking in to the $\phi$ distribution of all jets in every event, it is expected that the distribution of all jets for this variable is uniform. The distribution of this variable for the given baseline selection is given in Figure 4.2 (left). The quantity (Data - MC)/$\sigma$ indicates how many standard deviations $\sigma$ the number of data events differs from the MC simulated events, where $\sigma$ represents the systematic scaling uncertainty on the $t\bar{t}$ + jets sample. There are more uncertainties in play (e.g. stochastic uncertainties, pile-up ...), as will be discussed in Chapter 5, but the scaling uncertainty on the $t\bar{t}$ + jets sample is dominant.

The $\phi$ distribution is expected to be uniform for all samples as well as for data, so in order for the data to be in agreement with MC the values of (Data - MC)/$\sigma$ for each bin are expected to be uniform as well. Figure 4.2 (left) clearly indicates that some of the samples aren't well simulated for this baseline selection. In this case the disagreement is mainly caused by the Z + jets sample, being one of the two dominating backgrounds, as can be observed by looking at the distribution of the invariant mass of the two muon system in Figure 4.2 (right), with the invariant mass calculated as

$$M_{inv}^2 = 2p_{T1}p_{T2}(cosh(\Delta\eta) - cos(\Delta\phi)), \tag{4.5}$$

with $p_{T1}$ , $p_{T2}$ the transverse momenta of the two muons and $\Delta\eta$, $\Delta\phi$ the pseudo-raidity and $\phi$ seperation between both muons. In case the two muons come from the decay of a Z boson, the Z + jets distribution should be peaked around the Z mass $m_Z = 91.2$ GeV/c$^2$ [31]. Figure 4.2 (right) shows unexpected peaks at around 20, 30 and 40 GeV/c$^2$ for the invariant mass of the Z + jets sample. Thhis indicates that the simulated Z + jets sample does not have enough MC statistics for this baseline selection. In order for the disagreement to disappear, an extra cut will be made to reduce the Z + jets sample to a non-dominating background. As the decay $Z \to ll$ does not contain any neutrinos, the reconstructed MET for Z + jets events will be low and mainly due to bad MET resolution (3.3) instead of genuine MET. Most of the Z + jets events have a MET less than 50 GeV, so the extra selection criterion for every event is a minimum MET of 50 GeV.

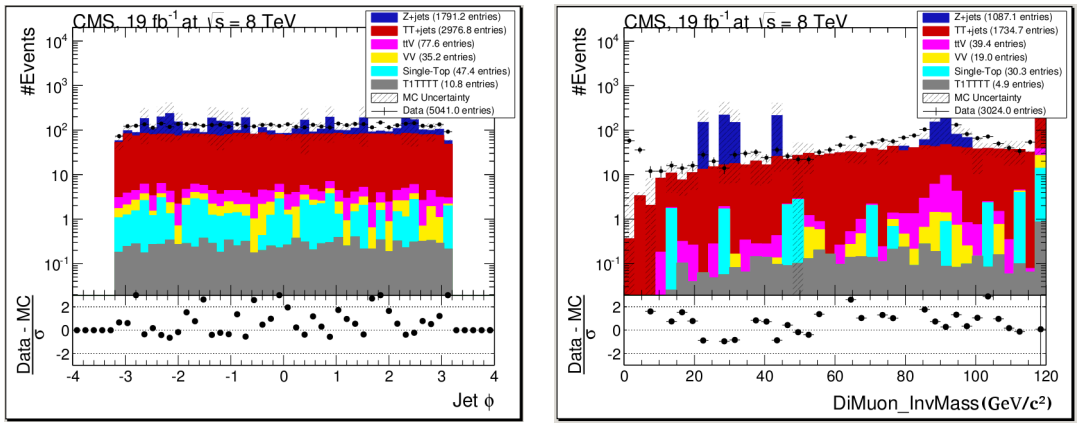


Figure 4.2: Left: the jet $\phi$ distribution before the MET cut is applied. Right: the invariant mass of the two muon system.

The distributions of the two control variables show a much better data to MC agreement after requiring each event to have MET $\geq$ 50 GeV, as shown in Figure 4.3, for the final baseline selection

$$\geq 5jets, \quad \geq 2b-tags, \tag{4.6}$$

$$MET \geq 50GeV.$$

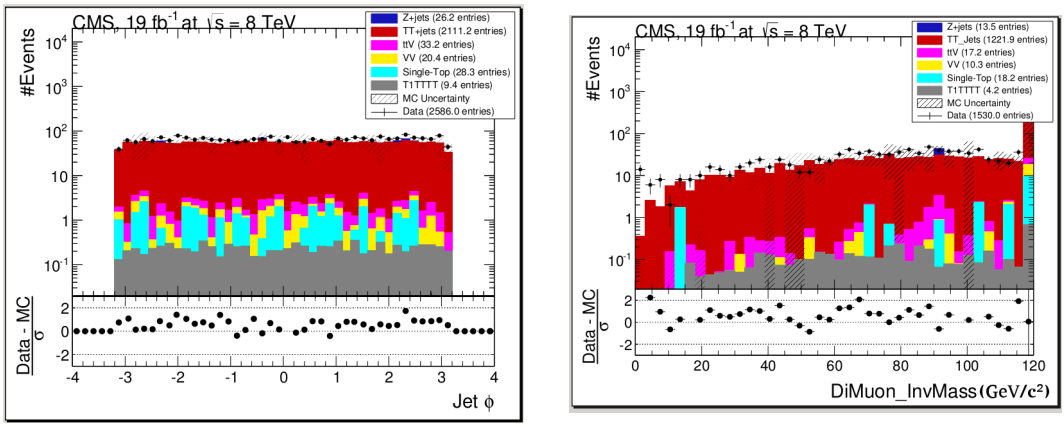


Figure 4.3: Left: the jet $\phi$ distribution after the extra MET requirement is applied. Right: the invariant mass of the two muon system after the extra MET requirement is applied.

The selection criteria have reduced one of the main backgrounds (Z + jets) to a level at which the number of events is comparable to the number of signal events, as can be seen in Table 4.4. Also the rare SM processes ($t\bar{t}V$, $W$, $SingleTop$ and $VV$) which were up to two orders of magnitude higher than the signal have been reduced to a negligible level (W + jets) or to a level comparable to the signal. However, one background process still dominates the final state, namely $t\bar{t}$ + jets (701 events).

Table 4.4: Selection table summarising the effect of the extra MET cut on the number of events for simulation and data for 18.83 $fb^{-1}$ of integrated luminosity.

| | $T1TTTT$ | $W+jets$ | $SingleTop+jets$ | $VV$ | $ttV$ | $t\bar{t}+jets$ | $Z+jets$ | $S/\sqrt{B}$ |
|---|---|---|---|---|---|---|---|---|
| $\geq$ 5 jets, $\geq$ 2 bTags, MET $\geq$ 50 GeV | 2.3 | 0.0 | 10.4 | 5.9 | 9.8 | 701.0 | 15.5 | 0.08440 |

The significance $S/\sqrt{B} = 0.08440$ is slightly improved compared to the significance when the baseline selection only consisted of two OS muons + at least five jets of which two are b-tagged ($S/\sqrt{B} = 0.06455$). However, the number of signal events can still be accomodated for by the Poissonian uncertainty on the background and therefore the kinematic properties of the signal will be further exploited to gain a higher signal sensitivity.

## 4.2 Multivariate analysis

Where other searches base their analyses on one specific kinematic variable ([50–52]), such as MET and the total activity in an event ($\sum E_T$), this analysis will look for additional variables where the differences in the kinematics of the simulated signal and background processes become apparent. This choice is strongly motivated by the fact that MET based variables are less discriminating in the compressed spectrum. Although this analysis is forced to use less discriminating variables due to the compressed scenario, by combining the information of several of these less discriminating variables, a 'master' discriminator can be constructed in which the discrimiation between signal and background is greater. This is known as a *Multivariate Analysis* (MVA). The MVA in this thesis is implemented using the *Toolkit* for *Multivariate Analysis* [56] (TMVA), which is a ROOT-integrated package for MVA.

In general an MVA consists of two steps.

- *training*: The training prepares the MVA by running over a subset (usually half) of the simulated samples and optimally combining the chosen variables into an event discriminator. The procedure of combining variables depends on the chosen MVA method.

- *computing*: In the computing part of the MVA, the whole data sample and the remaining half of the simulated samples is run over. In the computing part, the information from the training is used to calculate the discriminator value for each event.

It is very important to split the MC samples in two for training and computing to avoid overtraining. Overtraining means that the MVA learns and takes over statistical fluctuations from the training, which are different for other MC samples.

The separation power $S^2$ between signal and background of the MVA discriminator variable is defined [56] as

$$S^2 = \frac{1}{2}\int \frac{(\hat{m}_S(y) - \hat{m}_B(y))^2}{\hat{m}_S(y) + \hat{m}_B(y)} dy, \tag{4.7}$$

with $\hat{m}_S(y)$ ($\hat{m}_B(y)$) the probability for the signal (background) to have discriminator value y. The TMVA provides a method-specific ranking of all variables used in the MVA, according to their contribution to $S^2$.

### 4.2.1 Likelihood method

In this analysis the likelihood method is used to combine the variables. The method is based on the Neyman-Pearson lemma [57] for hypothesis testing, stating that the most powerful hypothesis test between two hypotheses ($H_0$ and $H_1$) is the *likelihood ratio* test. This lemma implies that (for non correlated variables) the likelihood MVA is the best performant MVA to discriminate signal from background. In the MVA likelihood method every single event is subjected to this hypothesis test, with the two hypotheses being $H_0$: the event is signal-like and $H_1$: the event is background-like. For the purpose of constructing a MVA likelihood discriminator, the definition of the likelihood ratio $R_L$ for an event i becomes

$$R_L(i) = \frac{L_s(i)}{L_s(i) + L_b(i)}, \tag{4.8}$$

with $L_s$ and $L_b$ respectively the signal and background likelihoods. This likelihood ratio differs from the one proposed in the Neyman-Pearson lemma, which is $R_L(i) = L_s(i)/L_b(i)$, but in order to limit the range of the ratio to a finite interval [0,1], the ratio is normalised to (4.8). The likelihoods are defined as the product of the probability density functions p of all variables included in the MVA

$$L_s(i) = \prod_k^N p_s(i), \qquad L_b(i) = \prod_k^N p_b(i), \tag{4.9}$$

with N being the number of variables.

A problem with the likelihood method is that it does not perform well with correlated variables, as it assumes the variables are uncorrelated. In high energy collisions many variables are correlated in some way (e.g. MET is correlated with the total activity in an event, as explained in Subsection 3.1.4). To avoid a bad performance of the likelihood, highly correlated variables will not be used in the procedure.

The ranking of variables in the likelihood MVA is obtained by calculating the *delta separation* for every variable 'i' as

$$\Delta S_i^2 = S_{full}^2 - S_i^2, \tag{4.10}$$

with $S_i^2$ the separation power (4.7) for all input variables, except variable 'i', and $S_{full}^2$ the separation power for the full set of input variables. The higher the delta separation, the more variable 'i' adds useful information to the likelihood discriminator. Negative delta separation means the likelihood discriminator performs better without variable 'i'.

### 4.2.2 Selection of variables

A large list of possibly discriminating variables was considered, containing variables such as MET, the transverse momenta of jets, but also less trivial variables, such as the transvere momentum of the system consisting only five jets and two OS muon. Three steps were considered in the selection of suitable variables for the MVA:

1. *Discriminating power*: Based on the discriminating power of every variable a decision is made whether to keep the variable for the next step in the selection. The discriminating power is determined by the overlap between the signal- and background distribution. The overlap factor is calculated by multiplying the normalised signal distribution with the normalised background distribution and taking the integral. If the overlap factor is bigger than 0.1 the variable will not be considered any further.

2. *Negative delta separation*: Variables with a negative delta separation are removed from the list.

3. *Correlation*: The correlations between variables are considered as well. Linear correlation coefficients $\rho$ between all variables in the list are calculated as
$$\rho(X,Y) = \frac{\sum_i (x_i - \bar{x})(y_i - \bar{y})}{\sqrt{\sum_i (x_i - \bar{x})^2 \sum_i (y_i - \bar{y})^2}}, \tag{4.11}$$
with $x_i$, $y_i$ the values of variables x and y for event 'i' and $\bar{x}$, $\bar{y}$ the means of these variables. The values of $\rho$ lie within the range [-1,1]. If two variables have a linear correlation of over 30% (i.e. $\rho$ not in [-0.3,0.3]), the lowest ranked variable will not be considered for the MVA. The 2-dimensional scatter plots have been investigated as well for any non-linear correlations. If two variables exhibit any kind of strong non-linear correlation in these plots, the lowest ranked variable is eliminated from the list. For the correlation scatter plots of the final list of selected variables, see Appendix A.

Several variables are based on the idea of combining two or more reconstructed objects by adding their four-momenta, in order to kinematically reconstruct their mother particle. The optimal combination of objects is chosen by requiring a minimal $\chi^2$-value
$$\chi^2 = \frac{(m_{comb} - m_{mother})^2}{\sigma^2_{mother}}, \tag{4.12}$$
with $m_{comb}$ the invariant mass of the combined objects, $m_{mother}$ the experimental mass of the mother particle as taken from [31] and $\sigma_{mother}$ the uncertainty on the experimental value.

In total seven variables passed the selection process and are considered as discriminating and uncorrelated. These seven variables are listed below with a physical explanation on how they discriminate signal from the main background ($t\bar{t}$ + jets). The distributions for signal and background for every one of these variables is shown in Figure 4.4. These distributions are normalised to the total number of events of their respective samples. Note that the jets are orderd according to their relative transverse momentum $P_T$, such that the first jet corresponds to the highest $P_T$ jet.

- $\Psi = \frac{P_T(3^{rd}Jet)+P_T(4^{th}Jet)}{P_T(1^{st}Jet)+P_T(2^{nd}Jet)}$: The first two jets tend to come from the LO process in $t\bar{t}$ + jets events, so these two jets should have a much higher transverse momentum than the third + fourth jet, which originate from NLO processes. In signal events however all jets up to even the eight jet, tend to be LO jets, i.e. jets coming directly from the top quark decay, resulting in a lower transverse momentum difference between the first two and following jets. So it is expected that the signal distribution is located at higher $\Psi$ values.

- $P_T(5^{th}Jet)$: The fifth jet in the $t\bar{t}$ + jets sample tends to come from NLO processes, thus more likely to have smaller momentum than LO jets. In the signal region the fifth jet tends to come from a top decay.

- $\Delta R_{(\mu 1,\mu 2)}$ (3.1): In the $t\bar{t}$ + jets sample the two muons tend to be back-to-back as they come from two decaying top quarks, which tend to decay back-to-back with respect to the $t\bar{t}$ reference frame. The back-to-backness results in a high $\Delta R$ separation. In signal events the muons are more likely to be randomly scattered in the detector as they may come from several top quarks decaying, which are not necessarily produced back-to-back with respect to the T1tttt reference frame.

- $\Delta R_{(jet1,jet2)}$ (3.1): In the $t\bar{t}$ + jets sample the two hardest jets tend to be back-to-back as they come from two decaying top quarks, which tend to decay back-to-back with respect to the $t\bar{t}$ reference frame. In signal events the two hardest jets are more likely to be randomly scattered in the detector as they may come from several top quarks decaying, which are not necessarily produced back-to-back with respect to the T1tttt reference frame.

- Centrality $= \frac{H_T}{P} = \frac{\sum^{AllJets} P_T}{||\vec{P}(\sum^{AllJets})||}$: The $H_T$ variable will be bigger for signal events than $t\bar{t}$ + jets events, because it contains more harder jets from top decays than the fully leptonically decaying $t\bar{t}$ + jets. By dividing $H_T$ with $P$ another effect is taken into account, namely the fact that particles coming from signal events are more likely to scatter in the central regions of the detector compared to $t\bar{t}$ + jets events. This is a direct result of the fact that the T1tttt system is much heavier than the $t\bar{t}$ + jets system. This results in a 'slower' T1tttt system, which will mainly decay in the central region of the detector, whereas the $t\bar{t}$ + jets system will be boosted more forwardly. It is therefore expected that the momentum of the vectorial sum of all jets, will be small for centrally dispersed jets and higher for forwardly dispersed jets.

- MET significance $= \frac{MET}{\sqrt{S_T}} = \frac{MET}{\sqrt{H_T+P_T(\mu 1)+P_T(\mu 2)+MET}}$: The di-leptonically decaying T1tttt system contains two neutrinos and two neutralinos, whereas the dileptonically decaying $t\bar{t}$ system only contains two neutrinos. Therefore the MET is expected to be larger in signal events than in $t\bar{t}$ + jets events. By dividing with $S_T$, which is a measure of the total activity in an event, the resolution (see Subsection 3.1.4) on the MET is accounted for.

- First reconstructed W mass = $m_{Di-jet}$ (the optimal combination of jets is chosen according to the least $\chi^2$ 4.12): In signal events, two W bosons are expected to decay hadronically, opposed to no hadronically decaying W bosons in $t\bar{t}$ + jets events. The distribution of the mass of a hadronically reconstructed W boson should therefore be sharply peaked around the W mass for signal, whereas the $t\bar{t}$ + jets sample will be more broadly distributed.

As it is clear from Figure 4.4 none of these variables are good standalone observables to discriminate signal from background, but when combined into one variable with a likelihood MVA the story changes.

The distributions for signal and background of the likelihood discriminator are shown in Figure 4.5 (left). These distributions are normalised to their respective total number of expected events. Figure 4.5 (right) shows the background rejection efficiency as a function of signal selection efficiency for the likelihood discriminator (blue) and the highest ranked variable from the list, $P_T(5^{th}Jet)$ (black). Such curves are referred to as *Receiver Operating Characteristic* curves (ROC) and are a good visualisation tool to determine the performance of a variable. Variables where the ROC curves get close to coordinate (1,1), are the most discriminating variables. This because that is the point at which 100% of the background events can be thrown away while keeping 100% of the signal events.

Figure 4.5 (left) shows that, although the signal is difficult to discriminate from background based on single kinematic variables (as becomes apparent in Figure 4.4, it is still possible to obtain a clear separation between signal and background by combining several less discriminating into a likelihood discriminator. This emphasises the succes of an MVA. Figure 4.5 (right) shows that the likelihood discriminator has a superior performance compared to a single kinematic variable, which motivates the idea to calculate an upper limit on the cross section based on the likelihood discriminator, instead of a single variable.

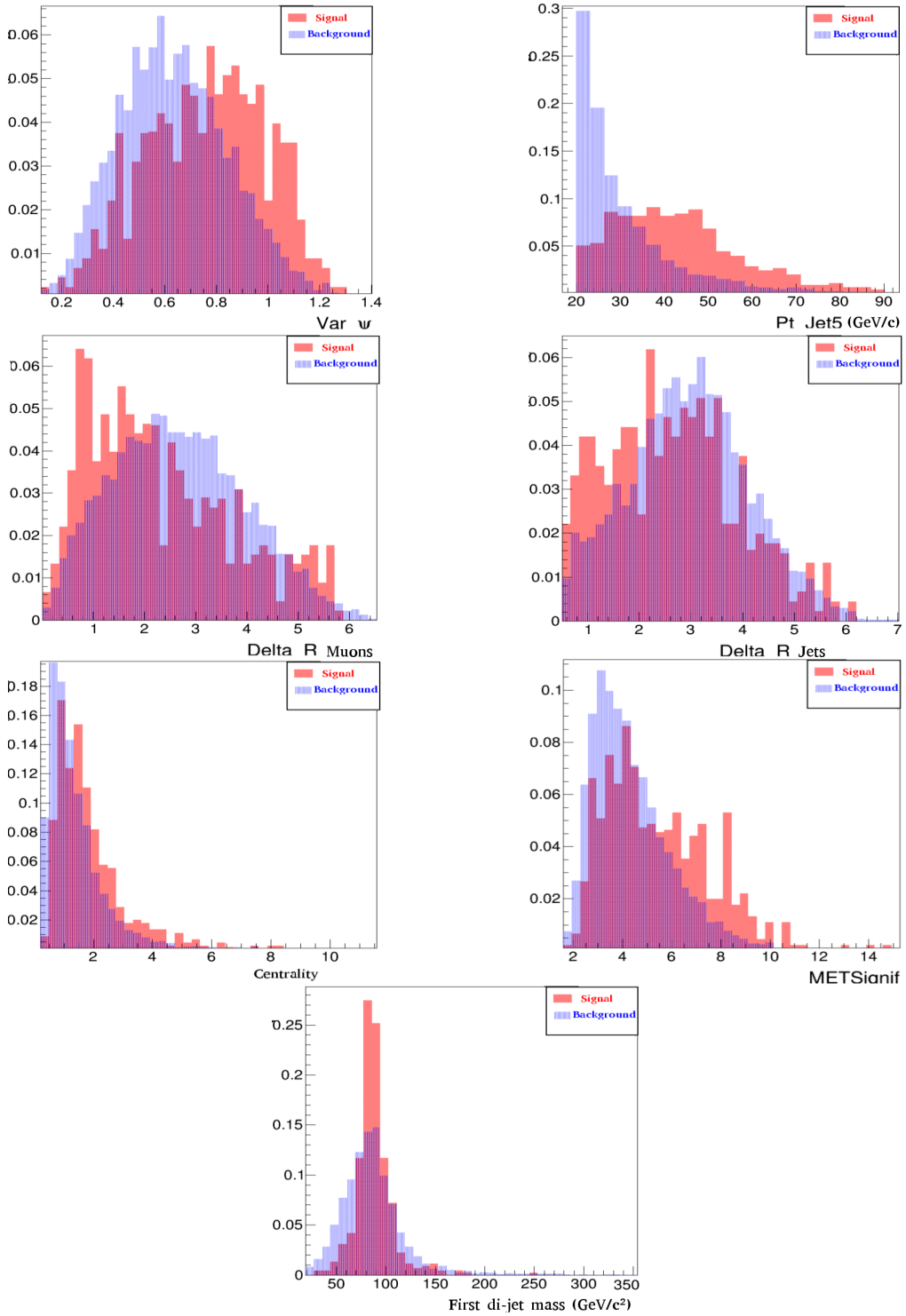


Figure 4.4: The distributions of the seven input variables for signal (red) and background (blue), normalised to their respective total number of events. The background consists of all background processes. The seven distributions are from left to right and top to bottom: $\Psi$, $P_T(5^{th}Jet)$, $\Delta R_{(\mu 1,\mu 2)}$, $\Delta R_{(jet1,jet2)}$, Centrality, MET significance and First reconstructed W mass.

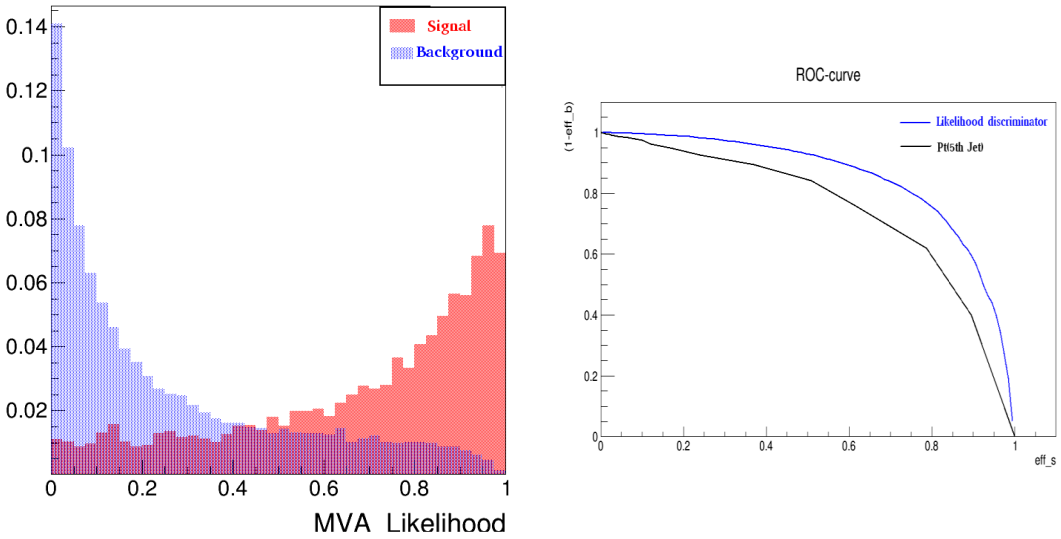


Figure 4.5: Left: the normalised distributions of the likelihood discriminator for signal (red) and background (blue). Right: ROC curve of the likelihood discriminator (blue) and $P_T(5^{th}Jet)$ variable (black).

# Chapter 5

# Calculation of limit on T1tttt cross section

In this chapter an upper limit on the considered T1tttt process will be calculated. This will be done by template fitting the likelihood discriminator distributions of signal and background to data.

## 5.1 Limit setting procedure

The calculation of an upper limit on the cross section of the T1tttt signal consists of a *template fitting* approach.

### 5.1.1 Template fitting

Template fitting starts from the assumption that the distribution of the likelihood discriminator variable in data may be modelled by the summation of template distributions from simulation. The procedure adopted in this analysis is template fitting the signal template distribution, added with the summed nominal background template distributions, to the data template distribution of the likelihood discriminator variable. In this procedure, the signal is scaled by a factor SigXsecOverSUSY. As SigXsecOverSUSY is a scaling of the simulated sample, it can be easily related to the theoretical cross section $\sigma_{SUSY}$ ($\sigma_{SUSY} = 25$ fb), which is used to create the simulated signal sample, as

$$SigXsecOverSUSY = \frac{\sigma_{signal}}{\sigma_{SUSY}}, \tag{5.1}$$

with $\sigma_{signal}$ the cross section of the signal according to the template fit. This parameter is referred to as the *parameter of interest*. However, from Section 3.2, it is known that the template distributions of simulations may be affected by systematic uncertainties. These uncertainties are treated as *nuisance parameters* in the template fit, since they are not the phenomena the analysis is looking for.

The procedure of estimating the contributions of the nuisance parameters and the parameter of interest to the data, will be discussed further. First an overview

is given of the systematic uncertainties that contribute as nuisance parameters to the template fit.

### Systematic uncertainties

As explained in Section 3.2 the MC simulations depend on a number of parameters, of which the nominal values come from theoretical predictions or experimental estimations. However these nominal values aren't known with 100% precision, so the precision with which these are known, gives rise to systematic uncertainties on the MC samples. Depending on what parameters are altered, the kinematics, jet-, b jet- and muon multiplicity can change in each sample.

A summary of all systematic uncertainties in this analysis, as introduced in Section 3.2, is given in Table 5.1. If the systematic uncertainty affects the shape of the distribution, it is indicated as a shape systematic. If, on the other hand, the systematic uncertainty only affects the overall scale of the distribution, it is indicated as a normalisation systematic. Only the overall effect on $t\bar{t}$ + jets events is given in Table 5.1 as it is the dominating background, with the overall effect calculated as

$$0.5\frac{N_+ - N_-}{N_{nominal}}, \tag{5.2}$$

with $N_\pm$ the number of expected events for $\pm$ 1 variation of the systematic uncertainty and $N_{nominal}$ the nominal expected number of events at an integrated luminosity of 18.83 $fb^{-1}$.

Table 5.1: Overview of the samples to which systematic uncertainties are considered, with the overall uncertainty of each uncertainty on the dominating background sample.

| Sources of systematic uncertainty | Type | Samples | Overall effect on $t\bar{t}$ |
|---|---|---|---|
| PU reweighting | Shape | All | 0.07 % |
| JEC | Shape | All | 1.4% |
| b-tagging efficiencies | Shape | All | 4.8% |
| Scaling | Shape | $t\bar{t}$ + jets | 15.7% |
| Parton-jet matching | Shape | $t\bar{t}$ + jets | 3.2% |
| Cross section | normalisation | $t\bar{t}$ + jets | 5.1% |
| Luminosity | normalisation | // | 4% |

The uncertainty on the recorded luminosity at CMS is taken from [58] and the uncertainty on the $t\bar{t}$ + jets process is taken from [49].

The scaling and matching uncertainty are only relevant for $t\bar{t}$ + jets events as this is the most dominant sample, where extra jets are created as QCD processes. The dominant uncertainty is the scaling uncertainty ($\sim$ 15.7%). This is due to the fact that the requirement of five jets implies that the dominating $t\bar{t}$ + jets is a

NNLO process. Such processes strongly depend on QCD perturbation calculations, which are regulated in simulation by scaling, thereby leading to a (relatively) large uncertainty on NNLO processes such as the $t\bar{t}$ + jets sample.

### Parameter estimation

The parameter estimation for the template fit of the likelihood discriminator variable is treated as a maximum likelihood estimation (MLE) [59]. The likelihood is defined as the joint probability

$$L(x_i|\vec{\theta}) = \prod_{i=1}^{n} f(x_i|\vec{\theta}), \tag{5.3}$$

with $f(x_i|\vec{\theta})$ the underlying probability density function (pdf) which is the probability to measure data point $x_i$ of the measured data set $X$=$\{x_0, .., x_n\}$, given the model nuisance parameters and parameter(s) of interest $\vec{\theta}$. So $L(x_i|\vec{\theta})$ gives the probability to measure data set $X$, given the model parameters $\vec{\theta}$, which are in this case the nuisance parameters and the parameter of interest. Usually the log of the likelihood is used in the MLE. The maximum likelihood method estimates the true underlying values of the parameters by requiring that for $\vec{\theta} = \hat{\vec{\theta}}$ the joint probability (5.3) achieves its maximum, i.e.

$$\hat{\vec{\theta}} \subseteq argmax_{\forall\vec{\theta}} log(L(x_i|\vec{\theta})), \tag{5.4}$$

i.e. it estimates the values of $\theta$ for which the likelihood is maximized. The MLE also calculates the uncertainty on every parameter, determined by the covariance matrix

$$cov(\theta_i, \theta_j) = -\frac{\partial^2 ln(L(x_i|\vec{\theta}))}{\partial\theta_i \partial\theta_j}|_{\vec{\theta}=\hat{\vec{\theta}}}. \tag{5.5}$$

In this case the the likelihood (5.3) is defined as [60]

$$L(X|\mu,\nu) = \prod_{i}^{n} \frac{e^{-\lambda_i(\mu,\nu)}\lambda_i^{x_i}(\mu,\nu)}{x_i!} \times \prod_{j}^{m} \pi_j(\tilde{\nu}_j|\nu_j), \tag{5.6}$$

with X = $\{x_1, .., x_n\}$ being the data set in terms of bin contents of the likelihood discriminator, $\mu$ the parameter of interest, $\nu = \{\theta_1, .., \theta_m\}$ the set of nuisance parameters, $\lambda_i$ a model dependent prediction of the number of expected events in bin 'i' and $\pi_j(\tilde{\nu}_j|\nu_j)$ the probability to assign a value $\tilde{\nu}_j$ to the nuisance parameter $\nu_j$ used in the model prediction. The first term in (5.6) corresponds to the product of Poissonian probabilities of observing $x_i$ events given the model prediction

$$\lambda_i(\mu,\nu) = \mu s_i(\nu_S) + b_i(\nu_B), \tag{5.7}$$

with '$s_i$' ('$b_i$') the number of expected signal (background) events in bin i and the subindices 'S' and 'B' indicating the nuisance parameters correlated to the signal

and background distribution. The second term constrains the values of the nuisance parameters $\nu_j$ according to their probabilities $\pi_j$, which are are parametrised by the systematic uncertainties described in in Subsection 5.1.1.

The whole maximum likelihood estimation depends on a large amount of parameters (34 systematic parameters + 25 statistical bin fluctuations). The computation is performed by MINUIT [61], which calculates the model predictions $\lambda_i$ and nuissance probabilities $\pi_j$ according to the likelihood discriminator variable obtained from the MVA. The MINUIT program maximizes the likelihood starting with a first estimation of the parameter values, evaluating the likelihood for this first estimations and calculating the covariances. Then it starts a second round, where it maximizes the likelihood for parameter values within the one $\sigma$ uncertainty interval from the first estimation. If this second round of MLE ends up in parameter and uncertainty values which do not differ from the first round, MINUIT stops and gives the values from the second round as final result of the MLE. However, if the results from the second round signifcantly differ from the first round, MINUIT continues to a next round and so on, until a round is reach where the resulting parameter values do not differ from the previous.

Figure 5.1 shows the resulting shape of the likelihood discriminator for the maximum likelihood estimated values. The $\pm$ one $\sigma$ uncertainty bands represent the extreme cases where all parameters simultaneously assume their $\pm$ one $\sigma$ value, which are determined according to (5.5).

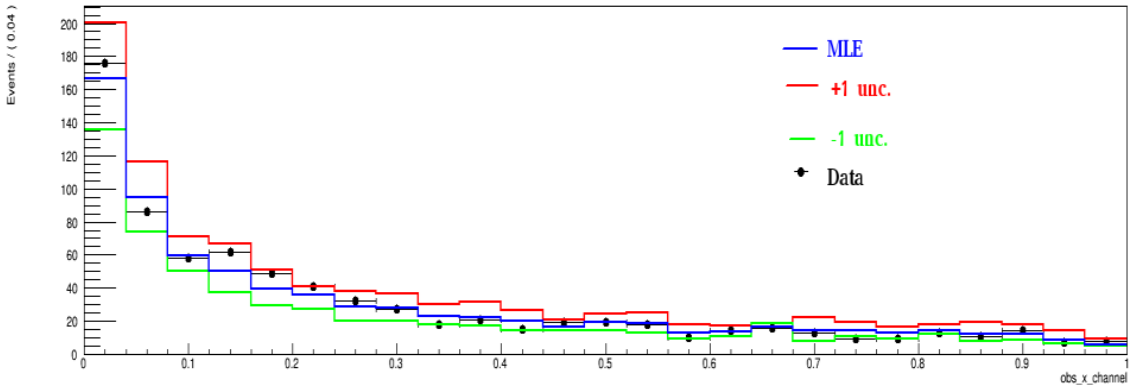


Figure 5.1: Visualisation of the resulting maximum likelihood estimation (MLE) for the likelihood discriminator variable. The indicated templates represent the best template fit (blue), and the two scenarios where all parameters simultaneously assume their $\pm$ one $\sigma$ value (red: upward shift, green: downward shift).

The maximum likelihood estimation for the value of the parameter of interest and its uncertainty interval (5.5) is

$$SigXsecOverSUSY = 0.606, \qquad [\sigma_-, \sigma+] = [0, 6.553]. \tag{5.8}$$

This value and its large uncertainty indicate that the probability for the signal to have no contribution to the data is as large as the probability that the signal is 6.5 times bigger than the predicted 25 fb. It is also a first indication that the data is

completely consistent with no signal contribution. This is due to the fact that the $t\bar{t}$ + jets sample has a large uncertainty, mainly dominated by the scaling systematic.

### 5.1.2 The CL$_s$ method

The likelihood discriminator will be used to produce an upper limit on the cross section of the signal. The general idea behind obtaining an upper limit on the cross section is based on hypothesis testing. The null hypothesis being that there is no signal and the alternate hypotheses corresponding to various signal cross sections ($\propto$ SigXsecOverSUSY). These hypotheses are evaluated according to a $test-statistic$ Q, which is a function of the parameter of interest $\mu$. The test-statistic Q is constructed such that its value increases for the observed dataset when $\mu$ increases. By comparing the value of the test-statistic Q on data with the expected test-statistic distributions for the null and alternate hypothesis, one can then either exclude or discover the signal. However instead of simply rejecting the null hypothesis in favour of the alternate hypothesis, a $confidence\ level$ (CL)[62] for exclusion (1-$\alpha$) is produced for every alternate hypothesis corresponding to a value of $\mu$. This means the alternate hypothesis can be rejected with a confidence of (1-$\alpha$)%. As soon as the confidence in the alternate hypothesis is smaller than 5% (i.e. CL $\leq \alpha = 0.05$), $\mu^{95\%}$ is excluded with 95% confidence. An upper limit on the cross section is obtained when for all values $\mu \geq \mu^{95\%}$, the corresponding confidence level is lower than 5%.

Depending on how sensitive the search is to the signal, different approaches are preferred. The approach adopted in this analysis is the $CL_s-method$ [63, 64]. The CL$_s$-method will be implemented as prescribed by ATLAS and CMS for the BEH boson search [65]. The used test-statistic is the profiled log-likelihood ratio (LLR)

$$Q_\mu(X) = \begin{cases} -2log\left(\frac{L(X|\mu,\hat{\nu}_\mu)}{L(X|\mu',\hat{\nu}_{\mu'})}\right) & \text{if } \mu \geq \mu' \geq 0 \\ 0 & \text{else,} \end{cases} \tag{5.9}$$

where the likelihood L is as defined in Subsection 5.1.1), $\mu$ is the parameter of interest and $\nu$ represents the whole set of nuisance parameters. The values for $\hat{\nu}_\mu$ are obtained by performing a maximum likelihood estimation for the specified value of $\mu$, whereas the values $\mu'$ and $\hat{\nu}_{\mu'}$ are the global fit values as obtained in Subsection 5.1.1. The larger the LLR the more data set X disagrees with $\mu$ as value for the parameter of interest compared to the predicted $\mu'$. The requirement of $\mu \geq \mu' \geq 0$ implies that the limit on SigXsecOverSUSY is one-sided, such that only upper limits are considered.

As the test-statistic depends on the data set X, it will assume different values for independent measurements. The distribution of these values, denoted as f($Q_\mu|\mu,\hat{\nu}_\mu$) assuming the measurement described by $\lambda(\mu,\hat{\nu}_\mu)$, is determined by conducting a number of toy experiments $X^T$. These toy experiments are performed by generating Poissonian-distributed numbers $x_i^T$ according to the $\lambda(\mu,\hat{\nu}_\mu)$ model, with $\hat{\nu}_\mu$ randomly generated according to the nuisance probabilities $\pi_j$. Then by evaluating the test-statistic for each of these toys, f($Q_\mu|\mu,\hat{\nu}_\mu$) is sampled and can be approximated. The more toy experiments, the better f($Q_\mu|\mu,\hat{\nu}_\mu$) is approximated,

but the more CPU time is required. In this analysis 1000 toy experiments are generated to sample the distribution.

From the test-statistic distributions the p-value[1] of the signal+background hypothesis is calculated as

$$p_{S+B}(\mu) = \int_{Q_\mu(X_{obs})}^{\infty} dQ_\mu f(Q_\mu|\mu, \hat{\nu}_\mu), \tag{5.10}$$

with $Q_\mu(X_{ref})$ the value of the test-statistic for the observed measurement $X_{obs}$ for the given value of $\mu$. Similar the p-value for the background-only hypothesis ($\mu = 0$) is calculated as

$$1 - p_B(\mu) = \int_{Q_\mu(X_{ref})}^{\infty} dQ_\mu f(Q_\mu|0, \hat{\nu}_0). \tag{5.11}$$

Figure 5.2 shows the test-statistic distributions for the background-only (blue) and signal+background (red) with SigXsecOverSUSY = 25. Also the value of the test-statistic on the real data is indicated.

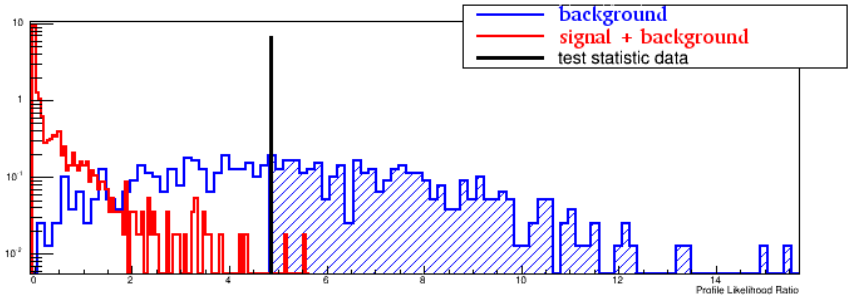


Figure 5.2: Distributions of the test-statistics for background (blue) and signal+background (red) for SigXsecOverSUSY = 25. The value of the test-statistic for the measured data set $X_{obs}$ is indicated as well.

According to these two p-values the confidence level for the $CL_s$ method is determined as

$$CL_s(\mu) = \frac{p_{S+B}(\mu)}{1 - p_B(\mu)}. \tag{5.12}$$

The $CL_s$-value is not strictly speaking a confidence level, but a ratio of confidences. If $CL_s(\mu) \leq \alpha$ the value $\mu$ is stated to be excluded with a confidence level of (1-$\alpha$). By taking the ratios of p-values for the signal + background hypothesis and background-only hypothesis, one takes into account that background fluctuations may mimic the $\lambda_i(\mu', \hat{\nu}_{\mu'})$ model. So the actual confidence level for the upper limit is higher than (1-$\alpha$). This is also the reason why the $CL_s$-method is preferred in a search where small signals are expected.

[1] The p-value is the traditional frequentist defined p-value and is to be interpreted as the probability to get a test-statistic at least as extreme as the observed one.

## 5.2 Results

In this thesis a scan is performed over different increasing values for $\mu$ (= SigXsecOverSUSY) using the $CL_s$-method. Figure 5.3 shows the resulting scan over 5 different values for SigXsecOverSUSY. The *observed limit* is obtained from the actual experiment, whereas the *expected limit* is obtained from simulated toy experiments. The expected limit indicates the limit one can expect to set, given the integrated luminosity of the dataset and the sensitivity of the analysis. The expected limit thereby shows how sensitive the analysis is to the signal, because as long as the signal can be accomodated by the background-only toy experiments, one can not confidently exclude the signal. The uncertainty on the expected limit (green and yellow bands) is large, mainly due to the scale uncertainty on the $t\bar{t}$ + jets sample.

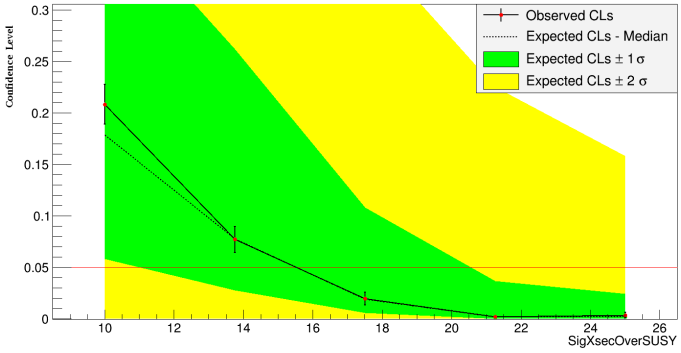


Figure 5.3: A $CL_s$ scan over the parameter of interest, with the observed limit for the real measured data set and the expected limit.

The expected limit is obtained by reproducing 1000 toy experiments for the background-only scenario ($\lambda(0, \hat{\nu}_0)$), with $\hat{\nu}_0$ generated according to the nuisance probabilities $\pi_j$. For every one of these background toy experiments the whole $CL_s$ procedure is repeated to obtain the 95% upper limit $\mu^{95\%}$. Then the mean from all these 1000 $\mu^{95\%}$ is calculated as

$$\frac{1}{2} = \int_{-\infty}^{\mu^{95\%}_{mean}} d\mu^{95\%} m(\mu^{95\%}), \tag{5.13}$$

with m($\mu^{95\%}$) being the underlying probability density for the $\mu^{95\%}$ background-only values. The uncertainty bands in Figure 5.3 are obtained by taking the statistical deviations from the mean $\mu^{95\%}_{mean}$ into account, such that they encompass 68% ($\pm 1\sigma$) and 95% ($\pm 2\sigma$) of the statistical fluctuations.

Figure 5.3 can now be intepreted that, as soon as the dashed line is below the red line (confidence level = 0.05) the experiment becomes sensitive to a signal with the corresponding value for SigXsecOverSUSY. If the dashed line is above the red line, the signal can not be excluded. As long as the observed $CL_s$ values are consistent with the expected values, the measured data set is completely consistent with the background-only hypothesis. Table 5.2 shows the corresponding 95% confident

upper limits for the observed and expected $CL_s$ procedure on SigXsecOverSUSY and the corresponding limit on the cross section, which can be calculated as in (5.1).

Table 5.2: 95% upper limits on SigXsecOverSUSY for the observed and expected case for a shape fitting analysis.

| | $SigXsecOverSUSY^{95\%}$ | cross section (fb) |
|---|---|---|
| Observed | 15.62 (± 0.81) | 391 (± 20) |
| Expected (mean) | 15.53 | 388.25 |
| Expected (-1 $\sigma$) | 10.98 | 274.5 |
| Expected (+1 $\sigma$) | 20.56 | 514 |
| Expected (-2 $\sigma$) | 1.32 | 33 |
| Expected (+2 $\sigma$) | 29.99 | 749.75 |

The analysis presented only becomes sensitive to a signal with a cross section of $388^{+125}_{-114}$ fb, as can be concluded from the expected limit in Figure 5.3 and the values from Table 5.2. As this cross section is 15.53 times bigger than the predicted cross section of 25 fb, the considered mass point for the T1tttt topology can not be completely excluded, nor is it discovered. However the calculated upper limit of the signal cross section, given the data recorded at the CMS experiment, is **391 fb** (± **20 fb**) as observed in the experiment. The $CL_s$ method has also shown that the recorded data set is completely consistent with the SM predictions for this specific final state with two opposite-sign muons, more than five jets of which two are b-tagged and more than 50 GeV missing transverse energy.

### Cut − and − count

As a simpler alternative to the template fitting approach, a cut-and-count analysis is presented, serving as a cross-check to the main analysis. This approach consists in finding an optimal cut in which the significance $S/\sqrt{B}$ is the highest for the signal. Then this cut is applied as an extra selection criterion for every event, beside the baseline selection. Then the $CL_s$ method is used to calculate an upper limit on the cross section, based on a scaling of the number of signal events to the data, given the number of background events. The template fitting method is preferred to the cut-and-count approach as main analysis, as more information is contained in the template distributions that is not optimally used in the cut-and-count approach. The cut-and-count analysis is based on one single counting experiment with one overall systematic uncertainty, whereas template fitting uses information of 25 seperate bins of which the uncertainties are better constrained according to several shape systematics, which can be varried seperately, next to two normalisation systematics.

In this cut-and-count approach the optimal cut is determined by looking at the effect of several cut values $c_{sign}$ in the likelihood discriminator variable on the

significance. The significance for several cut values $c_{sign}$ is shown in Figure 5.4 (left). From this plot it is determined that the most optimal cut is at $c_{sign} = 0.84$. Note however that is a simplified approach to a cut-and-count analysis, because the actual optimal cut may differ from this one when taking systematic effects into account. In total 41 data events, 30.8 simulated background events and 0.9 simulated signal events pass this cut, giving a signifcance of $S/\sqrt{B} = 0.166$. This significance is almost a factor of 15 better than the significance of the signal before even any selection on MET or number of jets was made ($S/\sqrt{B} = 0.01143$ taken from Table 4.3).

Based on these numbers and an overall systematic uncertainty of about 29% on the background, a $CL_s$ scan is performed over the SigXsecOverSUSY, as shown in Figure 5.4. This systematic uncertainty is obtained by applying all systematic effects seperately, then counting the number of background events passing the cut $c_{sign} \geq 0.84$. The total estimated systematic uncertainty is then

$$\sigma_i = \frac{|N_{syst,i} - N_{nominal}|}{N_{nominal}}, \tag{5.14}$$

with $N_{syst,i}$ the number of events passing the likelihood discriminator cut for the systematic distribution 'i' and $N_{nominal}$ the number of events passing the cut for the nominal distribution. The total uncertainty is than estimated as $\sigma_{total} = \sqrt{\sum_i \sigma^2_{sys,i}}$.

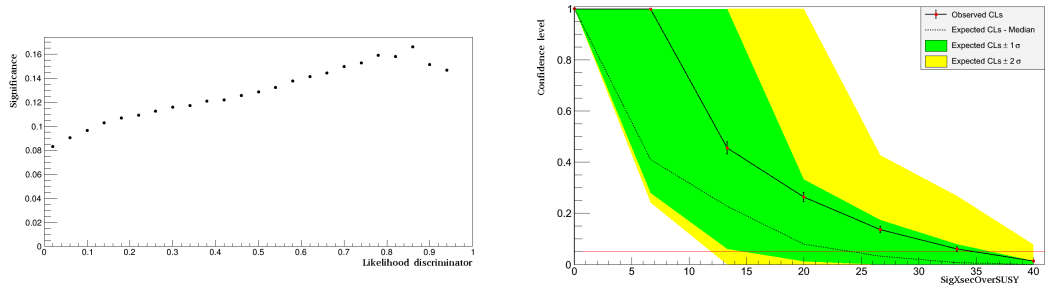


Figure 5.4: Left: The signifcance of the signal to the background uncertainty as a function of the applied cut. Right: $CL_s$ scan over SigXsecOverSUSY for the cut-and-count analysis.

Table 5.3 summarises the 95% upper limits for the cut-and-count analysis obtained from the $CL_s$-method.

The upper limits from the cut-and-count experiment are more than a factor of two higher than those obtained in the template fitting analysis. This confirms the idea that a template fitting approach performs much better than a cut-and-count analysis. The results from the cut-and-count are also consistent with those from the template fit.

Table 5.3: 95% upper limits on SigXsecOverSUSY for the observed and expected case for a cut-anc-count analysis.

| | SigXsecOverSUSY$^{95\%}$ | cross section (fb) |
|---|---|---|
| Observed | 34.8 ($\pm$ 2.1) | 870 ($\pm$ 53) |
| Expected (mean) | 24.31 | 607.75 |
| Expected (-1 $\sigma$) | 14.74 | 368.5 |
| Expected (+1 $\sigma$) | 36.30 | 907.5 |
| Expected (-2 $\sigma$) | 11.95 | 298.75 |
| Expected (+2 $\sigma$) | 41.02 | 1025.5 |

# Chapter 6

# Conclusions and outlook

This thesis aimed to look for the T1tttt topology as part of the Simplified Model Spectra in 18.83 fb$^{-1}$ of 8 TeV proton collision data recorded by CMS in 2012. Focused on a specific configuration for the masses of the gluino and neutralino ($m_{\tilde{g}} = 1050$ GeV/c$^2$ and $m_{\tilde{\chi}_1^0} = 650$ GeV/c$^2$), the analysis utilises the opposite-sign di-muon channel.As a part of the compressed spectrum, this specific T1tttt configuration is experimentally more challenging than uncompressed scenarios. This is due to the fact that the traditional variables, mainly depending on the MET of an event, do not discriminate the signal from background as well as in an uncompressed scenario, and due to the fact that this process has a very low cross section of 25 fb.

In order to obtain a higher signal significance, selection criteria were implemented in order to reduce the considered Standard Model background processes as much as possible while conserving most of the signal. These selection criteria consist of: exactly two opposite-sign muons, at least five jets, of which two are b-tagged and at least MET $\geq$ 50 GeV. This baseline selection resulted in an increased significance of $S/\sqrt{B} = 0.08440$ compared to the original significance of 0.01143 (with the requirement of exactly two opposite-sign muons). With these selection criteria there is only one dominant SM background process: $t\bar{t}$ + jets. In order to achieve optimum sensitivity for T1tttt signatures in compressed spectra, seven variables were selected based on the kinematic properties of the signal and the dominating background, which slightly differentiate the signal distribution from the background distributions. These seven variables were combined in to one discriminating 'master' variable, using an MVA based on the likelihood ratio. The resulting likelihood discriminator is, as shown in figure 4.5, far better performing than the best ranked variable implemented in the MVA, which confirms that it is indeed better to work with an MVA variable than with a traditional variable.

With this likelihood discriminator an upper limit on the cross section of the considered process was calculated in a template fitting approach using the CL$_s$-method (Chapter 5. The observed upper limit on the cross section of the T1tttt process with $m_{\tilde{g}} = 1050$ GeV/c$^2$ and $m_{\tilde{\chi}_1^0} = 650$ GeV/c$^2$, is **391 $\pm$ 20 fb**. The uncertainty on this limit is large, due to the fact that the scaling systematic uncertainty on the main simulated background process ($t\bar{t}$ + jets) is relatively large.

As a cross-check a cut-and-count analysis has been performed, which showed consistent results with the template fitting method, namely an observed upper limit on the signal cross section of **870 ± 53 fb**, as summarised in Table 5.3. As expected, the cut-and-count approach performs much worse than the template fitting analysis.

The outlook for the future is bright, because even though the signal is not excluded (nor discovered), the analysis is already sensitive to processes with a cross section of over $388.25^{+125.75}_{-113.75}$ fb. Keeping in mind that this analysis is set in only one of the opposite-sign dilepton channels ($\mu^+\mu^-$), it is to be expected that by expanding this analysis to the other opposite-sign dilepton channels (di-electron and electron + muon) the exclusion limits will slightly improve. However it is expected that by transferring the analysis to the same-sign dilepton, the limits will improve drastically, because there are but a few (low cross section) SM processe which can produce two same-sign leptons, reducing the $t\bar{t}$ dominant background to an ordinary background. This results in a much higher significance (see Table 4.2). For the moment, at the current recorded integrated luminosity of about 20 fb$^{-1}$, the limited statistics for same-sign leptons in data (about 30-40 events) suggests a cut-and-count approach is more suitable than a template fit analysis. If more statistics become available in the next round of proton collisions at the LHC in 2015, it will be interesting to do the same template fitting analysis in the same-sign dilepton channel to obtain improved exclusion limits. A similar improvement is to be expected when analysing the tri-lepton channel as well for T1tttt signatures.

# Bibliography


[1] M. E. Peskin and D. V. Schroeder, *An introduction to quantum field theory*. The Advanced Book Program. Addison-Wesley Publishing Company, 1995.

[2] F. Mandl and G. Shaw, *Quantum Field Theory*. A Wiley-Interscience publication. John Wiley & Sons, 2010.

[3] *Compact Muon Solenoid experiment at CERN's LHC*, `http://cms.web.cern.ch`.

[4] The CMS Collaboration, *Observation of a new boson with a mass near 125 GeV*, CMS-PAS-HIG-12-020.

[5] F. Englert and R. Brout, Phys. Rev. Lett. **13** (1964) 321–322.

[6] P. Higgs, Phys. Rev. Lett. **13** (1964) 508–509.

[7] E. Noether, Transport Theory and Statistical Physics **1** (1971), no. 3, 186–207.

[8] M. Kobayashi and T. Maskawa, Progress of Theoretical Physics **49** (1973), no. 2, 652–657.

[9] D. e. a. Andersson, Phys. Rep **97** (1983), no. 2, 31–145.

[10] A. Djouadi, Phys. Rept. **459** (2008).

[11] P. Langacker, Phys. Rept. **72** (1981), no. 185,.

[12] N. Polonsky, *Supersymmetry: Structure and Phenomena: Extensions of the Standard Model*. Lecture Notes in Computer Science. Springer, 2001.

[13] S. P. Martin, *A Supersymmetry primer*, `hep-ph/9709356`.

[14] D. Z. Freedman, P. van Nieuwenhuizen, and S. Ferrara, Phys.Rev. **D13** (1976) 3214–3218.

[15] G. Giudice and R. Rattazzi, Phys.Rept. **322** (1999) 419–499.

[16] G. L. Kane, C. Kolda, L. Roszkowski, and J. D. Wells, Phys. Rev. D **49** (Jun, 1994) 6173–6210.

[17] The CMS Collaboration, *Interpretation of Searches for Supersymmetry with Simplified Models*, CMS-PAS-SUS-11-016.

[18] L. Evans and P. Bryant, JINST **3 S08001** (2008).

[19] O. S. Brning, P. Collier, P. Lebrun, S. Myers, R. Ostojic, J. Poole, and P. Proudlock, *LHC Design Report*. CERN, Geneva, 2004.

[20] B. Aune, R. Bandelmann, D. Bloess, B. Bonin, A. Bosotti, M. Champion, C. Crawford, G. Deppe, B. Dwersteg, D. A. Edwards, H. T. Edwards, M. Ferrario, M. Fouaidy, P. D. Gall, A. Gamp, A. Gössel, J. Graber, D. Hubert, M. Hüning, M. Juillard, T. Junquera, H. Kaiser, G. Kreps, M. Kuchnir, R. Lange, M. Leenen, and M. Liepe, Phys. Rev. ST Accel. Beams **3** (Sept., 2000).

[21] *Compact Muon Solenoid experiment at CERN's LHC*, `http://home.web.cern.ch/`.

[22] The CMS Collaboration, JINST **3 S08004** (2008).

[23] The ATLAS Collaboration, JINST **3 S08003** (2008).

[24] The ALICE Collaboration, JINST **3 S08002** (2008).

[25] The LHCb Collaboration, JINST **3 S08005** (2008).

[26] The TOTEM Collaboration, JINST **3 S08007** (2008).

[27] The LHCf Collaboration, JINST **3 S08006** (2008).

[28] *CMS Physics Technical Design Report: Detector performance and software*. No. v. 1 in CMS Technical design report. CERN, 2006.

[29] R. Frhwirth, Nucl. Instrum. Methods Phys. Res., A **262** (1987).

[30] *Particle-Flow Event Reconstruction in CMS and Performance for Jets, Taus, and MET*, Tech. Rep. CMS-PAS-PFT-09-001, CERN, Apr, 2009.

[31] *Particle Data Group*, `http://pdg.lbl.gov/`.

[32] E. S. Davison, *Basics of QCD Perturbation Theory*, arXiv:0906.1833v2.

[33] G. P. Salam, *Towards Jetography*, arXiv:0906.1833v2.

[34] C. Weiser, *A Combined Secondary Vertex Based B-Tagging Algorithm in CMS*, Tech. Rep. CMS-NOTE-2006-014, CERN, Geneva, Jan, 2006.

[35] H. Pi, P. Avery, D. Green, J. Rohlf, and C. Tully, The European Physical Journal C - Particles and Fields **46** (2006), no. 1, 45–56.

[36] R. K. Ellis, W. J. Stirling, and B. R. Webber, *QCD and Collider Physics*. Cambridge University Press, 2003.

[37] *MadGraph*, `https://cp3.irmp.ucl.ac.be/projects/madgraph`.

[38] G. Altarelli and G. Parisi, Nucl.Phys. **298** (1977).

[39] Y. L. Dokshitzer, Sov.Phys. **641** (1977).

[40] V. N. Gribov and L. N. Lipatov, Sov.J.Nucl.Phys. **438** (1972).

[41] S. Catani, D. de Florian, M. Grazzini, and P. Nason, JHEP **0307** (2003) 028.

[42] T. Sjostrand, S. Mrenna, and P. Z. Skands, Comput.Phys.Commun. **178** (2008) 852–867.

[43] J. Allison *et al.*, Nuclear Science, IEEE Transactions on **53** (2006), no. 1, 270–278.

[44] *ROOT*, `http://root.cern.ch/drupal/`.

[45] K. Kirschenmann, J. Phys.: Conf. Ser. **404** (2012), no. 012013,.

[46] The CMS Collaboration, J. Instrum. **8 P04013** (Nov, 2012) P04013. 67 p. Comments: Submitted to the Journal of Instrumentation.

[47] *Re-weighting of events to account BTag efficiency and mistag scale factors*, `https://twiki.cern.ch/twiki/bin/view/CMS/BTagWeight`.

[48] *Apply SF for b/c/light tags to directly tagged jets in MC*, `https://twiki.cern.ch/twiki/bin/view/CMS/BTagSFUtil`.

[49] *Standard Model Cross Sections for CMS at 8 TeV.* , `https://twiki.cern.ch/twiki/bin/viewauth/CMS/StandardModelCrossSectionsat8TeV`.

[50] *Search for supersymmetry in final states with missing transverse energy and 0, 1, 2, 3, or at least 4 b-quark jets in 8 TeV pp collisions using the variable $\alpha_T$*, Tech. Rep. CMS-PAS-SUS-12-028, CERN, Geneva, 2012.

[51] *Search for gluino-mediated bottom- and top-squark production in pp collisions at 8 TeV*, Tech. Rep. CMS-PAS-SUS-12-024, CERN, Geneva, 2013.

[52] *Search for Supersymmetry in pp collisions at 8 TeV in events with a single lepton, multiple jets and b-tags*, Tech. Rep. CMS-PAS-SUS-13-007, CERN, Geneva, 2013.

[53] *Search for supersymmetry in events with same-sign dileptons*, Tech. Rep. CMS-PAS-SUS-12-017, CERN, Geneva, 2012.

[54] *A Search for Anomalous Production of Events with three or more leptons using 9.2 $fb^{-1}$ of $\sqrt{s}$ = 8 TeV CMS Data*, Tech. Rep. CMS-PAS-SUS-12-026, CERN, Geneva, 2012.

[55] T. J. LeCompte and S. P. Martin, *Large Hadron Collider reach for supersymmetric models with compressed mass spectra*, ANL-HEP-PR-11-32.

[56] A. Hocker, J. Stelzer, F. Tegenfeldt, H. Voss, K. Voss, *et al.*, PoS **ACAT** (2007) 040.

[57] J. Neyman and E. S. Pearson, *On the Problem of the Most Efficient Tests of Statistical Hypotheses*. Royal Society, 1933.

[58] The CMS Collaboration, *CMS Luminosity Based on Pixel Cluster Counting - Summer 2012 Update*, Tech. Rep. CMS-PAS-LUM-12-001, 2012.

[59] W. T. Eadie and J. Frederick, *Statistical Methods in Experimental Physics,*. World Scientific Publishing Company Incorporated, 2006.

[60] D. Falko and M. Bernhard, *Limit setting procedures and theoretical uncertainties in Higgs boson searches*, arXiv:1204.3851.

[61] *MINUIT*, `http://seal.web.cern.ch/seal/work-packages/mathlibs/minuit/`.

[62] P. Bock, JHEP **0701** (2007), no. 080,.

[63] A. L. Read, *Modified frequentist analysis of search results (the $CL_s$ method)*,.

[64] A. L. Read, Journal of Physics G: Nuclear and Particle Physics **28** (2002), no. 10 2693,.

[65] *Procedure for the LHC Higgs boson search combination in summer 2011*, Tech. Rep. ATL-PHYS-PUB-2011-011, CERN, Geneva, 2011.

# Appendix A

# Scatter plots

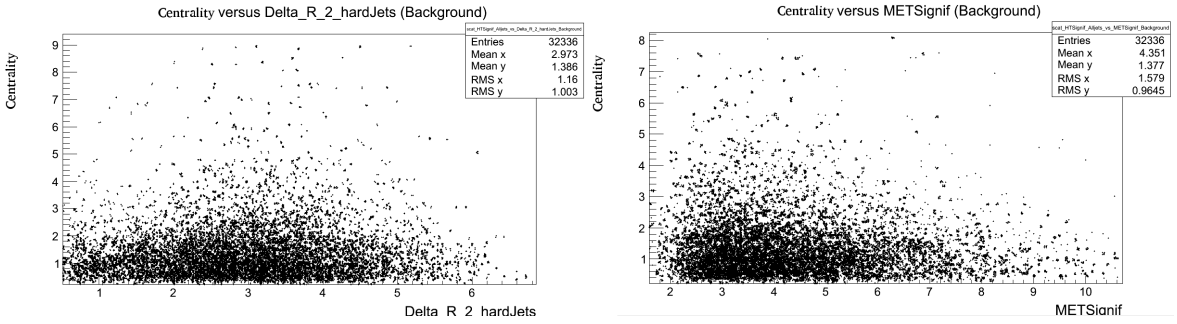


Figure A.1: 2D-scatter plots for background events. Left: Centrality versus $\Delta R_{(jet1,jet2)}$, right: Centrality versus MET significance.

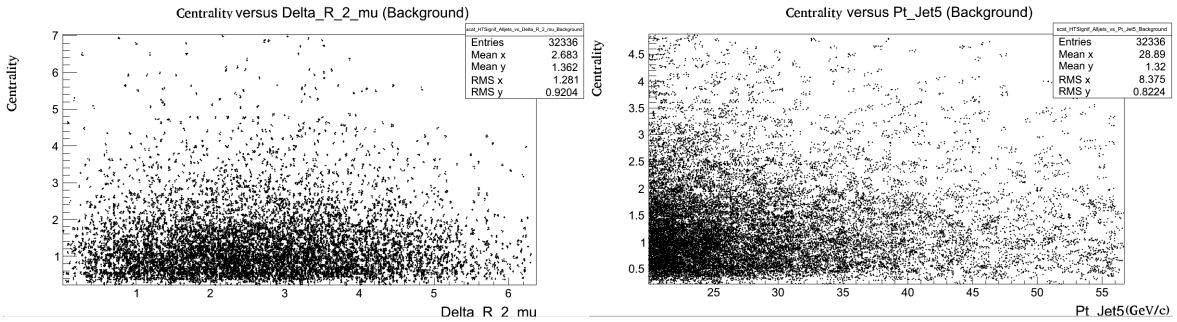


Figure A.2: 2D-scatter plots for background events. Left: Centrality versus $\Delta R_{(\mu 1,\mu 2)}$, right: Centrality versus $P_T(5^{th} Jet)$.

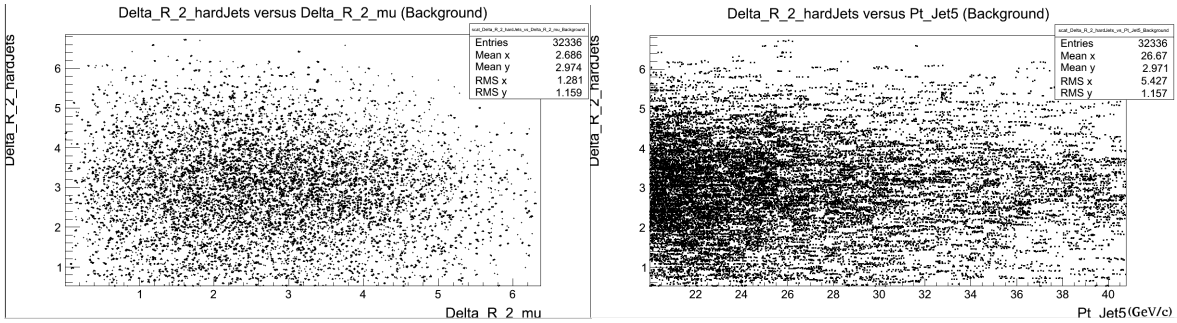


Figure A.3: 2D-scatter plots for background events. Left: $\Delta R_{(jet1,jet2)}$ versus $\Delta R_{(\mu 1,\mu 2)}$, right: $\Delta R_{(jet1,jet2)}$ versus $P_T(5^{th} Jet)$.

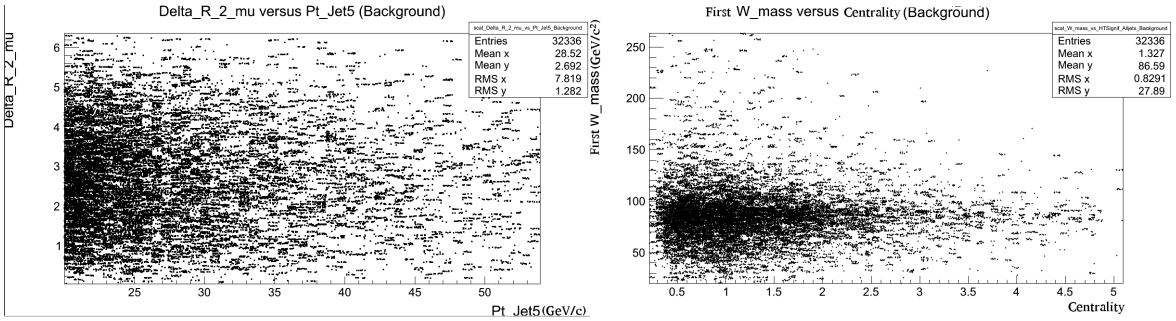


Figure A.4: 2D-scatter plots for background events. Left: $\Delta R_{(\mu 1,\mu 2)}$ versus $P_T(5^{th} Jet)$, right: First reconstructed W mass versus Centrality.

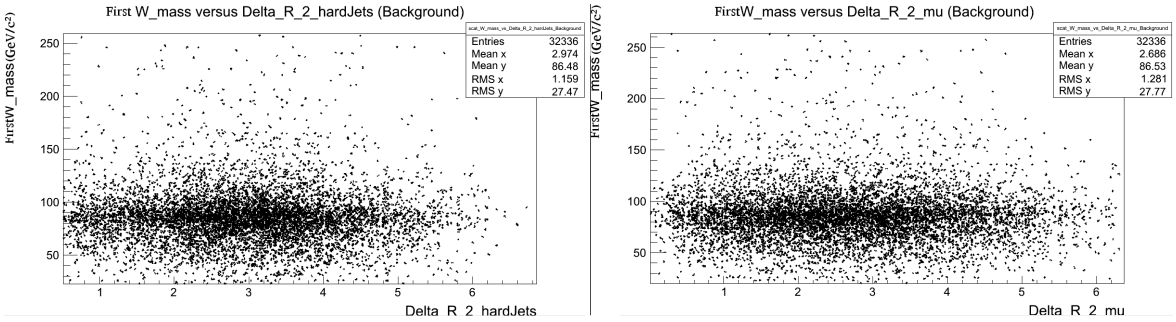


Figure A.5: 2D-scatter plots for background events. Left: First reconstructed W mass versus $\Delta R_{(jet1,jet2)}$, right: First reconstructed W mass versus $\Delta R_{(\mu 1,\mu 2)}$.

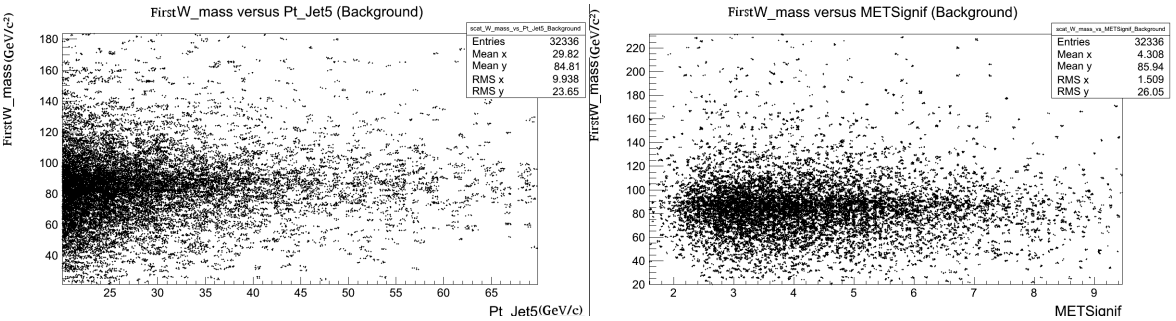


Figure A.6: 2D-scatter plots for background events. Left: First reconstructed W mass versus $P_T(5^{th}Jet)$, right: First reconstructed W mass versus MET significance.

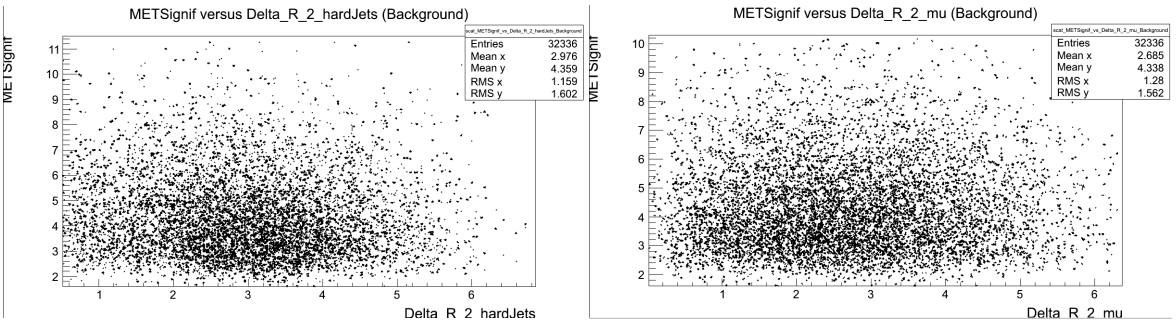


Figure A.7: 2D-scatter plots for background events. Left: MET significance versus $\Delta R_{(jet1,jet2)}$, right: MET significance versus $\Delta R_{(\mu 1,\mu 2)}$.

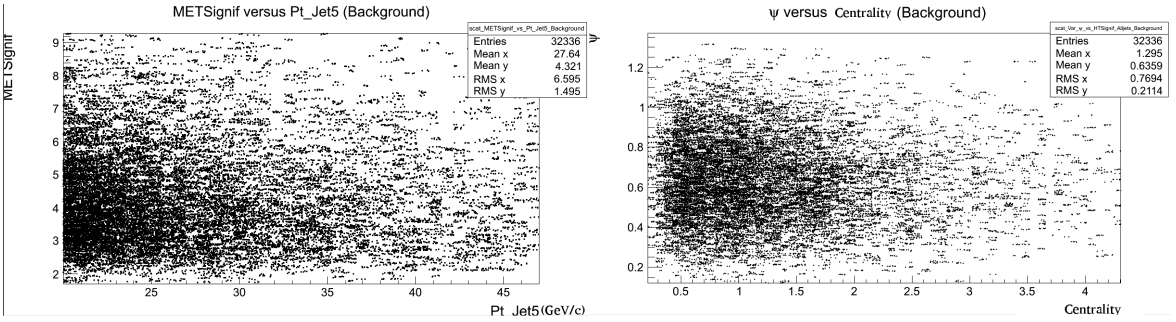


Figure A.8: 2D-scatter plots for background events. Left: MET significance versus $P_T(5^{th}Jet)$, right: $\Psi$ versus Centrality.

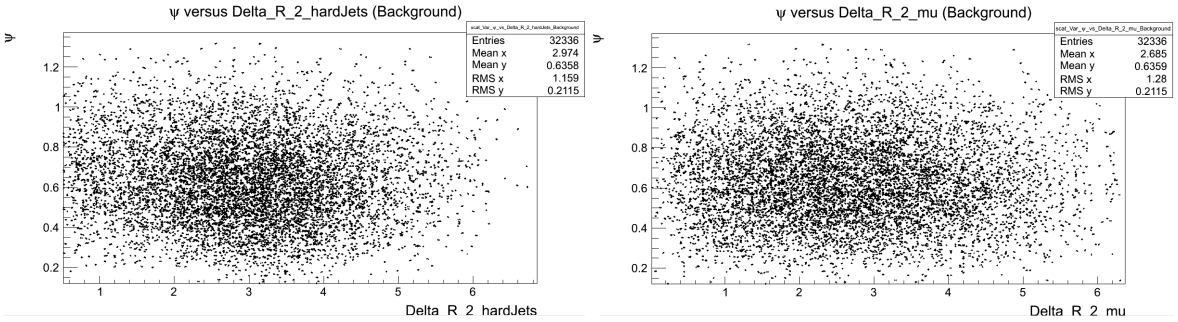


Figure A.9: 2D-scatter plots for background events. Left: $\Psi$ versus $\Delta R_{(jet1,jet2)}$, right: $\Psi$ versus $\Delta R_{(\mu 1,\mu 2)}$.

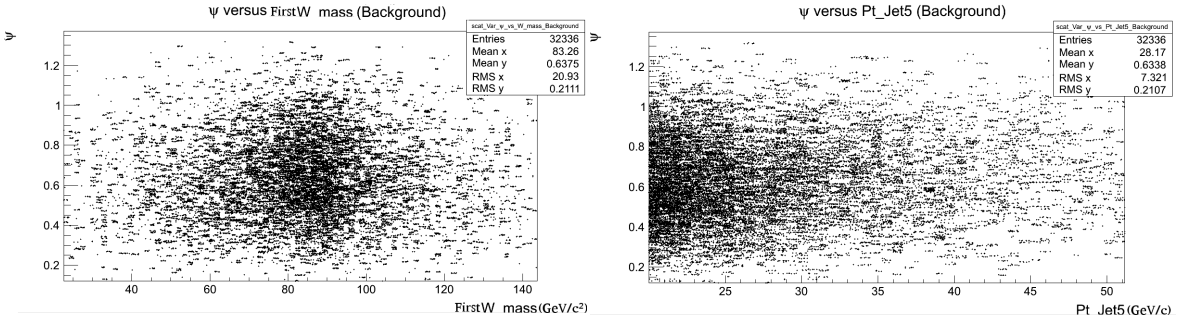


Figure A.10: 2D-scatter plots for background events. Left: $\Psi$ versus First reconstructed W mass, right: $\Psi$ versus $P_T(5^{th} Jet)$.

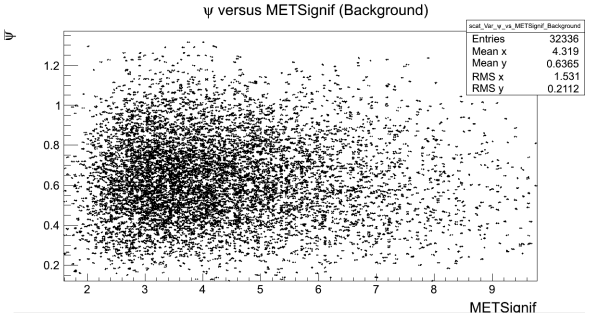


Figure A.11: 2D-scatter plots for background events, $\Psi$ versus MET significance.

# Summary

The Standard Model describing elementary particles and their interactions, being recently finalized with the discovery of the Brout-Engler-Higgs boson, exhibits a large amount of failures as it comes to explaining the hierarchy problem, unification of coupling constants, the presence of dark matter, CP violation... One has to resort to new fundamental physics theories that could accomodate the failures of the Standard Model. Out of the many theories proposed as an extension to the Standard Model, Supersymmetry (SUSY) looks the most promising as it provides solutions to the hierarchy problem, unification of coupling constants and dark matter, by introducing a whole series of new particles. If such SUSY particles exist, detectable signatures may be produced in energetic collisions, such as in proton collisions at the Large Hadron Collider in CERN.

This thesis presented a procedure to search for SUSY signals in the kinematics of final state topologies with four top quarks produced in 18.83 fb1 of 8 TeV proton collision data recorded by CMS in 2012 The analysis focused on one specific aspect of SUSY processes, namely the T1tttt process where two heavy gluinos $\tilde{g}\tilde{g}$ ($\mathrm{m}_{tildeg}$ = 1050 GeV/c$^2$) are produced. Each gluino undergoes a three-body decay $\tilde{g} \rightarrow t\bar{t}\chi_1^0$, with $\chi_1^0$ a neutralino ($m_{\tilde{\chi_1^0}}$ = 650 GeV/c$^2$), thus producing a final state containing four top quarks. This specific SUSY configuration is part of the compressed spectrum, due to the relatively small mass difference between the gluino and neutralino, and has a low predicted cross section of 25 fb. These two properties of the investigated process pose experimental challenges and require a two step approach. First of all, in order to increase the significance of the signal to Standard Model background processes such as diboson production, baseline selection criteria are implemented. These baseline selectio criteria require exactly two opposite-sign muons, more than 50 GeV missing transverse energy and at least five jets, of which two are b-tagged. The second step consisted of combining seven different variables in to one 'master' variable, using a likelihood Multivariate Analysis, in which the difference between the signal distribution and Standard Model background distributions becomes more apparent than in a single kinematic variable.

The likelihood discriminator is then used in a template fit to obtain an upper limit on the cross section of the signal process. The observed upper limit, calculated with the CL$_s$ method, on this specific T1tttt configuration, is **390.5 ± 20.35 fb**. This result is consistent with a simple cut-and-count analysis for which the observed upper limit is much higher (869.75 ± 53.25 fb). This cut-and-count result also indicates that in this case, where a low signal significance is expected, a template fitting analysis performs better than a simple cut-and-count analysis.

# Samenvatting voor deskundigen

## Een zoektocht naar supersymmetrie in het vier top quark kanaal van het CMS experiment

Het Standaard Model dat de elementaire deeltjes en hun interacties beschrijft, recentelijk gefinaliseerd met de ontdekking van het Brout-Englert-Higgs boson, vertoont een groot aantal tekortkomingen die tot uiting komen in het hiërarchie probleem, de eenmaking van koppeling constantes, de aanwezigheid van donkere materie, CP schending, etc. Om deze tekortkomingen van het Standaard Model te verklaren, moet men nieuwe fundamentele fysica theorieën beschouwen die complementair zijn aan het Standaard Model. Van de vele voorgestelde theorieën als aanvulling op het Standaard Model is Supersymmetrie (SUSY) een van de meest beloftevolle theorieën, omdat deze oplossingen biedt voor het hiërarchie probleem, de eenmaking van koppeling constantes en donkere materie, door een nieuwe collectie fundamentele deeltjes te introduceren. Indien zulke SUSY deeltjes bestaan, kunnen deze detecteerbare signalen produceren in energetische botsingen, zoals in proton botsingen aan de LHC te CERN.

Deze thesis omvat een procedure om SUSY signalen te zoeken in de kinematica van eindtoestand topologieën met vier top quarks, die geproduceerd worden in 8 TeV proton botsingen opgetekend in het CMS experiment in 2012 met een geïntegreerde luminositeit van 18.83 fb[1]. De analyse is geconcentreerd op een specifiek aspect van SUSY processen, namelijk het T1tttt proces waar twee zware gluinos $\tilde{g}\tilde{g}$ ($\mathrm{m}_{tildeg} = 1050$ GeV/c$^2$) worden geproduceerd. Elke gluino ondergaat een drielichaams verval $\tilde{g} \to t\bar{t}\chi_1^0$, met $\chi_1^0$ een neutralino ($m_{\tilde{\chi_1^0}} = 650$ GeV/c$^2$), waarbij een eindtoestand met vier top quarks ontstaat. Deze specifieke SUSY configuratie is onderdeel van het gecomprimeerd spectrum, omwille van het relatief kleine massa verschil tussen de gluino en het neutralino, en heeft een laag voorspelde werkzame doorsnede van 25 fb. Deze twee eigenschappen van het onderzocht process stellen experimentele uitdagingen en vereisen een aanpak in twee stappen. Ten eerste, om de significantie van het gesimuleerde signaal ten opzichte van de gesimuleerde Standaard Model achtergrond processen te vergroten, worden een aantal selectie criteria geïmplementeerd. Deze selectie criteria bestaan uit: exact twee tegengesteld geladen muonen, meer dan 50 GeV ontbrekende transversale energie en tenminste vijf jets, waarvan er twee gemarkeerd zijn als b-jets. De tweede stap bestond erin om zeven verschillende variabelen te combineren, gebruik makend van een waarschijnlijkheids Multivariate analyse, tot een 'meester' variabele, waarin het verschil tussen de signaal verdeling en de achtergrond verdelingen duidelijker wordt dan in een enkele

kinematische variabele.

Deze waarschijnlijkheids discriminator wordt dan gebruikt om de verdelingen van de simulaties te vergelijken met de verdeling van de data in een zogenaamde 'template fit'. Zo wordt een bovenlimiet bepaald op de werkzame doorsnede van het signaal proces. De geobserveerde bovenlimiet op deze werkzame doorsnede, voor deze specifieke configuratie van T1tttt, is **390.5 ± 20.35 fb**. Dit resultaat is consistent met een simpele snij-en-tel analyse waarvoor de geobserveerde bovenlimiet veel hoger ligt (869.75 ± 53.25 fb). Dit snij-en-tel resultaat toont ook aan dat in dit geval, waar de signaal significantie zeer laag is, een template fit beter presteert dan een snij-en-tel analyse.

# Samenvatting voor deskundigen

## Een zoektocht naar supersymmetrie in het vier top quark kanaal van het CMS experiment

De fundamentele deeltjes waaruit materie is opgebouwd en hun onderlinge interacties worden beschreven door het Standaard Model van de deeltjesfysica. Dit model slaagt erin om de zwakke, sterke en electromagnetische krachten succesvol te bundelen in een consistente theorie. Hoewel dit model zeer accurate voorspellingen deed die experimenteel bevestigd werden, zoals het bestaan van quarks als fundamentele bouwstenen van protonen en neutronen, schiet het model op andere vlakken dan weer zwaar te kort. Zo slaagt het er niet in om ook de vierde fundamentele kracht, de zwaartekracht, in de theorie in te bouwen, maar kan het ook geen verklaringen geven voor bepaalde waargenomen fenomenen, zoals bijvoorbeeld het bestaan van donkere materie en de ongelijke verdeling tussen materie en anti-materie in het universum. Om deze fenomenen te verklaren, worden er nieuwe theorieën opgesteld als aanvulling op het Standaard Model. Een van deze theorieën, namelijk supersymmetrie, ziet er veelbeolovend uit Deze theorie kan door het introduceren van een hele reeks nieuwe fundamentele deeltjes het donkere materie probleem en de meeste andere problemen van het Standaard Model oplossen. Indien zulke supersymmetrische deeltjes bestaan, kunnen deze detecteerbare signalen geven in energetische botsingen, zoals in de proton botsingen in de LHC.

Deze thesis presenteert een procedure om te zoeken naar supersymmetrische signalen in proton botsingen geregistreerd aan het CMS experiment, waarin vier top quarks geproduceerd worden als eindtoestand. Het supersymmetrisch productie mechanisme dat in deze thesis onderzocht wordt, is een zeer zeldzaam proces dat moeilijk te onderscheiden valt van de enorme hoeveelheid Standaard Model gebeurtenissen. Door middel van een hele resem selectie criteria wordt het aantal Standaard Model gebeurtenissen zoveel mogelijk gereduceerd met behoud van het supersymmetrisch proces. Uiteindelijk wordt ook gebruik gemaakt van de kinematische eigenschappen, namelijk de energie, massa en snelheid, van het supersymmetrisch proces, om experimenteel een bovenlimiet te stellen op de productie van zulke supersymmetrische deeltjes.

# Acknowledgements

First of all I would like to thank my promotors Jorgen D'Hondt and James Keaveney for the discussion sessions in which new insights were gained, which inspired me to optimize the analysis. An extra special thanks goes to James for his guidance and assistence throughout the whole year and the constructive feedback regarding the analysis. His experience really benefitted my analysis. In extension I would like to thank the whole team at the IIHE, for sharing in their know-how regarding experimental particle physics and its CPU aspects that facilitated my thesis.

I would like to thank my parents for supporting me throughout the my whole academic carreer and giving me the chance to complete my studies in tranquillity. Finally I would also like to thank my betrothed for encouraging me and accepting that the past months the thesis got my undivided attention.